ABSTRACT

Title of Dissertation: HIGH FIELD OPTICAL NONLINEARITIES
IN GASES

Yu-Hsiang Cheng, Doctor of Philosophy, 2013

Directed By: Professor Howard M. Milchberg,
Department of Physics and
Electrical and Computer Engineering

Optical femtosecond self-channeling in gases, also called femtosecond filamentation, has become an important area of research in high field nonlinear optics. Filamentation occurs when laser light self-focuses in a gas owing to self-induced nonlinearity, and then defocuses in the plasma generated by the self-focused beam. The result of this process repeating itself multiple times is an extended region of plasma formation. Filamentation studies have been motivated by the extremely broad range of applications, especially in air, including pulse compression, supercontinuum generation, broadband high power terahertz pulse generation, discharge triggering and guiding, and remote sensing.

Despite the worldwide work in filamentation, the fundamental gas nonlinearities governing self-focusing had never been directly measured in the range of laser intensity up to and including the ionization threshold. This dissertation presents the first such measurements. We absolutely measured the temporal refractive index change of O_2, N_2, Ar, H_2, D_2 and N_2O caused by high-field ultrashort optical pulses with single-shot supercontinuum spectral interferometry, cleanly separating for the first time the instantaneous electronic and delayed rotational nonlinear response in diatomic gases.

We conclusively showed that a recent claim by several European groups that the optical bound electron nonlinearity saturates and goes negative is not correct. Such a phenomenon would preclude the need for plasma to provide the defocusing contribution for filamentation. Our results show that the ‘standard model of filamentation’, where the defocusing is provided by plasma, is correct.

Finally, we demonstrated that high repetition rate femtosecond laser pulses filamenting in gases can generate long-lived gas density ‘holes’ which persist on millisecond timescales, long after the plasma has recombined. Gas density decrements up to ~20% have been measured. The density hole refilling is dominated by thermal diffusion. These density holes will affect all other experiments involving nonlinear high repetition-rate laser pulse energy absorption by gases.

HIGH FIELD OPTICAL NONLINEARITIES IN GASES

By

Yu-Hsiang Cheng

Dissertation submitted to the Faculty of the Graduate School of the
University of Maryland, College Park, in partial fulfillment
of the requirements for the degree of
Doctor of Philosophy
2013

Advisory Committee:
Professor Howard M. Milchberg, Chair
Professor Christopher C. Davis
Professor Ki-Yong Kim
Research Scientist John P. Palastro
Professor Amy S. Mullin (Dean's representative)

Acknowledgments

First of all, I am deeply grateful to my advisor, Prof. Howard Milchberg, who introduced me to the world of ultrafast, high-field laser-matter physics. It would have never been possible for me to finish all the work described in this thesis without his mentorship and insightful advice about experiments.

I wish to express gratitude to Dr. Jared Wahlstrand, who is glad to share his wisdom and collaborated with me on many great scientific research projects.

I would like to acknowledge the other colleagues, Dr. Yu-Hsin Chen, Dr. Sanjay Varma, Dr. Brian Layer, Nihal Jhajj, Sina Zahedpour, Eric Rosenthal, Arman Fallahkhair, George Hine, Reuven Birnbaum, Jennifer Elle, Sung Jun Yoon, Andrew Goers, Colin Kennedy, for their technical assistance and fruitful discussions. It is a wonderful pleasure to work with them.

My sincere thanks also go to Jay Pyle, Stephen Henderson and Nolan Ballew for the help of machining.

In the end, I am deeply indebted to my parents, my younger brother, and my wife, Yi-Yuan, for their strong spiritual support.

Table of Contents

List of Tables

List of Figures

Chapter 1

Physics and applications of high field optical nonlinearities in gases: introduction and overview

1.1 Optical nonlinearities in gases

The nonlinear optical response of gases plays an important role in a variety of phenomena under wide investigation for applications, including harmonic generation and attosecond physics [1], femtosecond filamentation [2], and pulse compression [3].

The total response is composed of instantaneous and delayed parts, which are, respectively, the nonlinear distortion of the atomic or molecular electron cloud (electronic response) and field-induced molecular rotation, with a weak, fast contribution from adiabatic (prompt) bond stretching. Together, these responses are called the optical Kerr nonlinearity.

In molecular gases, for excitation pulses with duration of 100 fs or longer, the delayed molecular alignment response is more important — even dominant — compared to the prompt electronic response [4]. The delayed response can be expressed by a convolution integral of excitation $I(t)$ and temporal Raman response function $R(t)$. The total temporal refractive index change $\Delta n(t)$ is

$$\Delta n(t) = n_2 I(t) + \int_{-\infty}^{t} I(t')R(t-t')dt', \tag{1.1}$$

where $n_2 I(t)$ is the instantaneous nonlinear response, n_2 is called the Kerr coefficient or nonlinear refractive index, $I(t)$ is the temporal profile of the laser pulse intensity. Therefore, in atomic gases (which only have electronic response) $\Delta n(t)$ follows $I(t)$. $R(t)$ includes the polarizability anisotropy $\Delta\alpha$ (defined as $\Delta\alpha = \alpha_{\parallel} - \alpha_{\perp}$, where $\alpha_{\parallel}$ and $\alpha_{\perp}$ are the linear polarizabilities along and across the molecular bond axis, respectively), rotational constant B ($B = \hbar/(4\pi c I_M)$, I_M is moment of inertia) and nuclear spin statistics [5].

The instantaneous response is often given in terms of $\chi^{(3)}$, which is the third-order optical nonlinear susceptibility. The relation between n_2 and $\chi^{(3)}$ is introduced as follow.

In linear optics or the low-field regime, the field-induced dipole moment per unit volume, or polarization density is described by $P(t) = \chi^{(1)}E(t)$, where $\chi^{(1)}$ is linear susceptibility and $E(t)$ is the amplitude of the applied electric field. In nonlinear optics or the high-field regime, $P(t)$ is expressed as

$$P(t) = \left(\chi^{(1)}E(t) + \chi^{(2)}E^2(t) + \chi^{(3)}E^3(t) + \cdots\right), \tag{1.2}$$

where $\chi^{(m)}$ ($m \geq 2$) is called the mth order nonlinear susceptibility. Note that in the above expressions of $P(t)$, we have assumed that the material response is instantaneous. This is because in our pump-probe experiments, the photon energy of pump and probe beams are 1.55 and ~2 eV respectively, which are well below the resonances of the studied gases even for third-order nonlinear processes, thus the optical response of material can be regarded as dispersionless. From the Fourier transform, we know that a nearly flat response in the frequency domain implies a δ-

function-like response in the time domain; that is, $\chi^{(3)}(t-t_1,t-t_2,t-t_3) \approx \chi^{(3)}\delta(t-t_1)\delta(t-t_2)\delta(t-t_3)$.

In this thesis, we focus on centro-symmetric material, in which $\chi^{(2)}=0$. With the definition $E(t)=\frac{1}{2}\left(E_0(t)e^{-i\omega t}+c.c.\right)$, where $E_0(t)$ is the slowly varying field envelope of $E(t)$, ω is the carrier frequency and $c.c.$ stands for complex conjugate, the time averaged intensity is $I=\frac{n_0 c}{8\pi}|E_0(t)|^2$. By considering the contribution to polarization from the fundamental frequency ω only, we write $P(t)=\frac{1}{2}\left(P_0(t)e^{-i\omega t}+c.c.\right)$, where $P_0(t)$ is the slowly varying envelope of $P(t)$. Through Eq. 1.2 we get

$$P_0(t)=\left(\chi^{(1)}+\frac{3}{4}\chi^{(3)}|E_0(t)|^2\right)E_0(t)=\chi_{\text{eff}}E_0(t), \tag{1.3}$$

where χ_{eff} is effective susceptibility.

Without considering the delayed part, we write the refractive index as $n=n_0+n_2 I$, where n_0 is the linear index of refraction and $n_2 I \ll n_0$, thus $n^2 \approx n_0^2+2n_0 n_2 I$. Because $n^2=1+4\pi\chi_{\text{eff}}$ and $n_0^2=1+4\pi\chi^{(1)}$, via eq. 1.3 we obtain the relation between n_2 and $\chi^{(3)}$:

$$n_2=\frac{12\pi^2\chi^{(3)}}{n_0^2 c}. \tag{1.4}$$

Many techniques have been used to estimate or infer the nonlinear refractive index of gases, including measurements of self-focusing [6], spectral changes caused by self-phase modulation [7, 8], and pump-probe experiments measuring spectral or polarization changes in a weak probe pulse due to cross-phase modulation [9-11]. Despite the extensive activity employing nonlinear laser-gas interactions, the Kerr nonlinearity, especially in molecular gases, is still not known with much precision.

Commonly used values for the instantaneous and delayed contributions to the Kerr nonlinearity vary significantly [7, 10-12]. Improving the precision of these numbers is critical for calculations of the propagation of intense laser pulses in gases, which depend extremely sensitively on them [13-17].

Shelton and Rice [12] obtained the nonresonant, electronic second hyperpolarizability γ ($\gamma = \frac{n_2 n_0^2 c}{12\pi^2} = \chi^{(3)}$), and its dispersion in gases by measuring the second harmonic generation induced in a symmetry breaking static electric field, which is the third-order nonlinear process $2\omega = \omega + \omega + 0$. Nibbering *et al.* [7] made high-intensity unfocused 120 fs pulses propagate through low-pressure gases and obtained n_2 by analyzing the self-phase-modulated spectra. Loriot *et al.* measured the transient birefringence in N_2, O_2, Ar and air, and extracted n_2 by fitting the theoretical calculations of signal to the experimental data at low pump intensity [10, 11].

Bridge and Buckingham obtained $\Delta\alpha$ by means of measuring the depolarization ratio of Rayleigh-scattered light of a helium-neon gas laser at low gas pressure [18].

In chapter 2, we introduce single-shot supercontinuum spectral interferometry (SSSI) [19-21], which enables the measurement, with micron spatial resolution and femtosecond time resolution, of the time-dependent phase imparted to a probe pulse by the transient response of a medium excited by a copropagating pump pulse. In this thesis, the SSSI technique with excellent spatial and temporal resolution is essential for measuring n_2 and $\Delta\alpha$.

In chapter 3, clean separations of the instantaneous electronic and delayed rotational responses of gases will be presented. This separation and the precise determination of interaction length (detailed in sec. 3.2) enable absolute measurement of n_2 and $\Delta\alpha$.

1.2 Introduction to laser filaments

Filamentation of femtosecond laser pulses in gases is an area of wide and increasing interest owing to applications such as harmonic generation, supercontinuum generation, and the possibility of generating greatly extended plasma conducting channels [2]. Filaments are produced by the interplay between self-focusing induced by the bound electron nonlinearity in the atoms or molecules of the gas and defocusing from the plasma generated by the self-focused laser light. Liu *et al.* found that the low intensity background energy reservoir surrounding the filament core region is crucial to filament propagation and its length [22]. A simplified conceptual picture of filament formation is shown in Fig. 1.1.

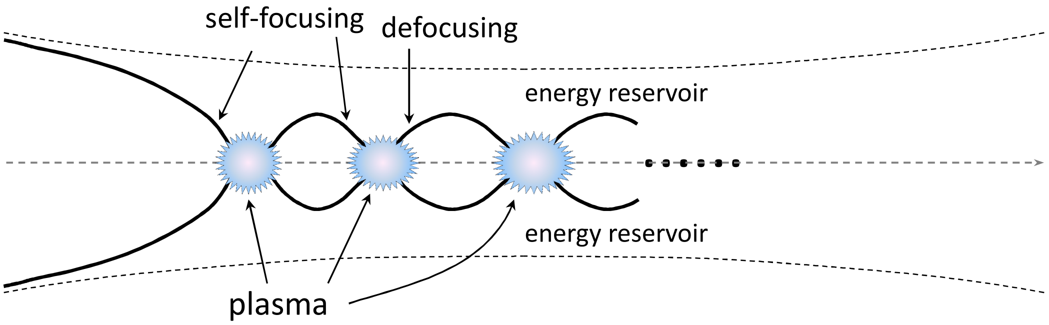

Figure 1.1 A simplified conceptual picture (modified from [2]) of the focusing–defocusing model of filamentation. The high intensity core region is shown with solid lines. The dashed lines represent the case without multiple recurrences of self-focusing and defocusing.

Varma *et al.* confirmed that for temporal pulse widths > 100 fs, the major air nonlinearity contributing to filamentation is the molecular alignment to field polarization [17, 23]. Later, it was shown that with the two-pulse excitation scheme that makes use of the quantum wake (formed by the coherent sum of molecular rotational states) of the first pulse, one can significantly enhance the filament propagation distance [24, 25]. Furthermore, it was demonstrated with simulations of pulse propagation in air that multiple femtosecond pulses separated by the proper delays (around a rotational revival period of N_2) can lead to pulse compression, spectral broadening or increased collimation [26].

Chen *et al.* directly measured the on-axis electron density of single filaments [17] with the scheme of shallow pump-probe grazing angle and the folded wavefront interferometric imaging (introduced in sec. 2.5). The results disagree with the hypothesis of plasma-free filamentation [10, 11] (introduced in sec. 1.3).

Typically, millijoule-level optical laser pulses are sufficient for extended filaments. A common application of filaments is broad frequency spectrum generation and pulse shortening [2, 27-32] in sealed gas cells, where the laser driver is a high pulse repetition rate system, which can typically range up to 5 kHz.

In 2001, Tzortzakis *et al.* reported electric discharges triggered and guided by infrared femtosecond laser pulses in air [33]. Thus, this technique has the potential to be used for lightning protection and control [34]. They observed nanosecond and microsecond timescale discharge guiding respectively in two different experimental configurations. Although the mechanism of the *delayed* guiding is still not completely understood, it is believed that the formation of a gas density depression channel at the center of the filament path plays an important role: a heated air column undergoes radial hydrodynamic expansion, and then the resulting, delayed, low-density column has a lowered breakdown threshold (the Paschen law) [33], providing a specific path for discharge [34].

1.3 The debate on the higher order Kerr effect (HOKE)

A recent transient birefringence measurement in the components of air reported by Loriot *et al.* [10, 11] purported to show that the optical Kerr effect saturates and then becomes negative for intensities greater than 43 / 25 / 34 / 34 TW/cm^2 in N_2 / O_2 / Ar / air, respectively, as shown in Fig. 1.2, where $n_{Kerr\parallel}$ is the instantaneous nonlinear refractive index change along the pump polarization direction. A new mechanism called the higher-order Kerr effect (HOKE) was proposed by these authors to explain their result. In the HOKE model, $n_{Kerr\|} = n_2 I + n_4 I^2 + n_6 I^3 + n_8 I^4 + n_{10} I^5$ for Ar and $n_{Kerr\|} = n_2 I + n_4 I^2 + n_6 I^3 + n_8 I^4$ for N_2, O_2 and air, where the higher order coefficients n_4, n_6, n_8, and n_{10} are obtained from fitting their data to the model [10, 11] and have alternating signs. Where this nonperturbative polynomial is truncated is determined by the number of photons required to ionize the studied gas in a multiphoton ionization process [35].

A strong higher-order Kerr effect, with a crossover from positive to negative nonlinear index at intensities well below the ionization threshold, would have a huge impact on the nonlinear optics of transparent media and has inspired theoretical works predicting plasma-free light filamentation [36] and exotic new effects in light propagation [37]. It would overturn the picture most have of the mechanism behind long-range filamentary propagation of intense ultrashort pulses—as arising from an interplay between self-focusing due to the positive optical nonlinearity from bound electrons and defocusing due to the plasma generated by ionization. The existence of a higher-order Kerr effect would also have implications for the general nonlinear susceptibility in transparent media [38, 39], including harmonic generation [40-42].

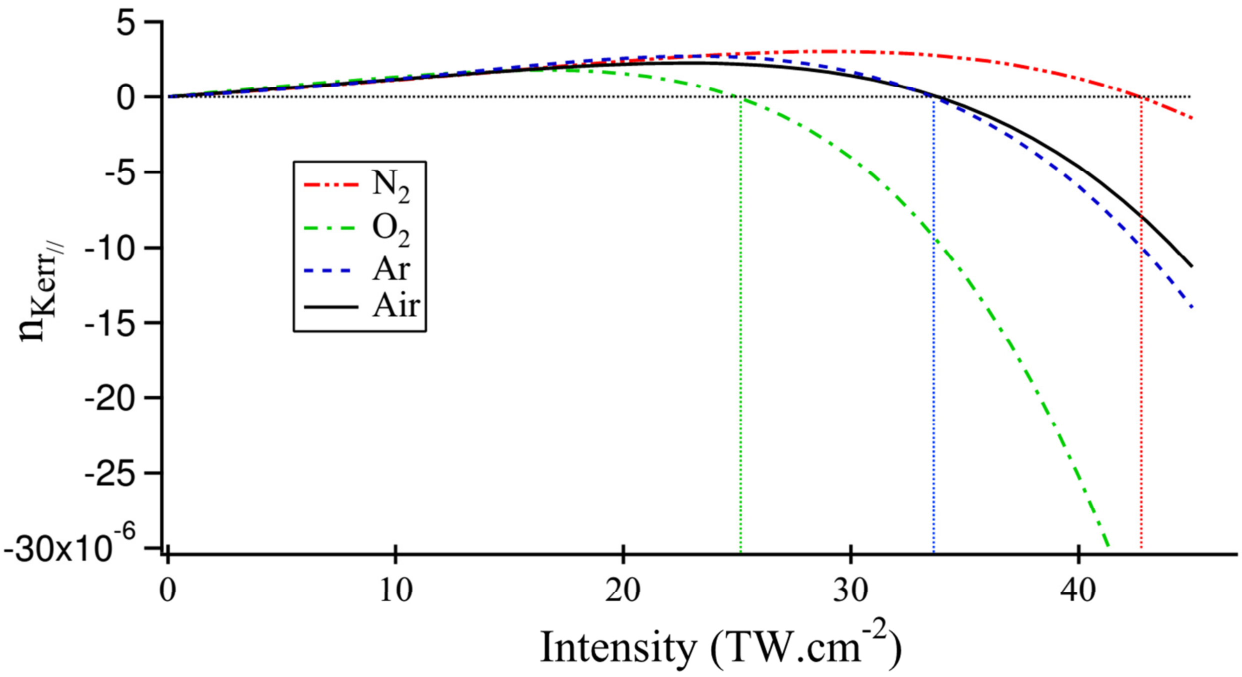

Figure 1.2 The instantaneous nonlinear refractive index variation along the pump polarization direction ($n_{Kerr\|}$) of air constituents versus the pump intensity obtained by the transient birefringence experiment at room temperature and 1 atm [10, 11].

Subsequent experimental studies of light filaments [17, 40, 43, 44] have not supported the higher-order Kerr model, with one exception [45]. One measurement [17] found that the electron density was 2 orders of magnitude higher than predicted by a calculation including higher-order nonlinearities but agreed with a simulation based on plasma defocusing alone [36]. In the earlier measurements using supercontinuum spectral interferometry [20], 110 fs pump pulses were used to study the optical nonlinearity of major air components, and no evidence of sign reversal of the instantaneous nonlinear refractive index was observed until at the intensities where ionization takes place. A physical mechanism for the saturation and negative response was proposed based on the nonlinear response near the threshold of ionization [46, 47].

What was missing from this debate was a direct measurement of the nonlinearity that corroborated or refuted the intensity dependence observed by Loriot *et al.* In chapter 4, to further study the controversy, we present such a measurement in noble gases and N_2 using spectral interferometry, and show that the instantaneous nonlinear phase shifts are all linear in the intensities up to the ionization thresholds [48, 49]. We find no saturation and no negative instantaneous nonlinear phase, in contrast to the original experiment [10].

In addition, the plasma grating theory proposed by Wahlstrand *et al.* [50, 51] gives an alternative explanation for Loriot's experiment, and our degenerate, parallel-polarized pump-probe experiment in Ar corroborates this theory [51]. Odhner *et al.* measured spectrally resolved transient birefringence in air and Ar with 400 nm / 800 nm pulses [51, 52]; and the results also support the plasma grating theory.

1.4 Laser-induced long timescale gas dynamics and its effect on femtosecond filamentation

In an experiment (not part of this dissertation) to measure time-resolved laser ionization of gases at a fraction of atmospheric pressure using our spectral interferometry diagnostic, we found that the ionization yield varied with the pump repetition rate. Compared to the 1 kHz case, full ionization (electron density ~ the gas density before the gas is hit by laser pulses) appeared to be achieved only when lower repetition rate (20 Hz) is applied. This puzzling effect was resolved by doing interferometry on the target gas, whereupon we discovered that pump pulses at 1 kHz generated a significant gas density depression that persisted on sufficiently long time scales that successive pulses at 1 kHz experienced the accumulated density depression contributed to by all the preceding pulses. At 20 Hz, the time between pump pulses was long enough for the density depression to dissipate.

Chapter 5 describes in detail our study of these gas density depressions. We showed that femtosecond filaments can generate long-lived, radially localized and axially extended depressions in the gas density that gradually dissipate via thermal diffusion on a millisecond timescale. The effect was significant even with pulse energies as low as ~100 μJ. At sufficiently high laser pump repetition rates, we found that the long timescale gas dynamics can strongly influence the propagation of pulses in the pulse train.

The drop in gas density caused by heating from nonlinear absorption of the laser (for example, via multi-photon ionization [2] or 2-photon Raman excitation of molecular rotation [53]) is thought to play a role at the <100 ns timescale in the triggering of electrical discharges by filaments [33, 54], but to our knowledge the very long time scale behavior had not been recognized to affect filamentation at high pulse repetition rates.

Chapter 2

Laser system, experimental chamber, and diagnostics

2.1 Description of the laser system

Here, a brief overview of the laser system is provided. The high energy laser pulses used in the experiments of this dissertation are generated with a commercial 1kHz Ti:sapphire regenerative amplifier (RA) (Coherent Legend Elite HE) seeded by mode-locked pulses centered at 800 nm from a Coherent Mantis oscillator. The laser output at 1 kHz is 3.5 mJ per pulse with a minimum pulse duration of ~38 fs.

In the oscillator, negatively-chirped mirrors are used for balancing the dispersion from material (mainly Ti:sapphire crystal) and self-phase modulation. In addition, there is a glass wedge added for fine tuning the net dispersion. The well-controlled net dispersion helps to obtain stable mode-locking.

A cavity mirror is mounted on a solenoid-driven spring to initiate Kerr lens mode-locking (KLM). A strong disturbance from the vibrating mirror will cause beating between longitudinal modes of different frequencies, so that KLM can be initiated by the most intense mode-beating pulse [55].

Prior to injection into the RA, the seed pulse is temporally stretched by a grating stretcher to avoid damage caused by high peak power induced self-focusing. Then it circulates in the RA cavity (round-trip time ~10 ns) and gets amplified within 15 passes through the Ti:Sapphire crystal. The pulse injection and ejection from the RA is controlled by Pockels cells synchronized to the oscillator pulses.

Finally, after exiting the RA cavity, the pulse is compressed to its shortest duration with a compressor composed of a horizontal retroreflector, single grating and vertical retroreflector. The horizontal retroreflector is mounted on a motorized stage so that the amount of chirp can be tuned freely in both directions.

The beam size (FWHM) at the RA output is 4.0 mm and the minimum pulse width is ~38 fs, measured with a home-built single-shot optical autocorrelator.

2.2 Introduction to Single-shot Supercontinuum Spectral Interferometry

Single-shot supercontinuum spectral interferometry (SSSI) [4, 19-21, 48] is a pump-probe technique for measuring ultrafast transients in the refractive index of excited materials. The desired information is encoded in the interferogram of two replica supercontinuum (SC) pulses in the spectral domain.

The two SC pulses are delayed by time τ such that the first pulse (the 'reference' pulse) precedes the pump and the second pulse (the 'probe' pulse) overlaps the pump. Before co-propagating the probe and reference SC pulses into the medium with the pump, they are stretched in time and chirped with a thick piece of glass or a prism pair to increase their duration up to ~2 ps. This makes possible a temporal field of view up to ~2 ps for measuring refractive index transients in a single shot.

The SSSI experimental setup is shown in Fig. 2.1.

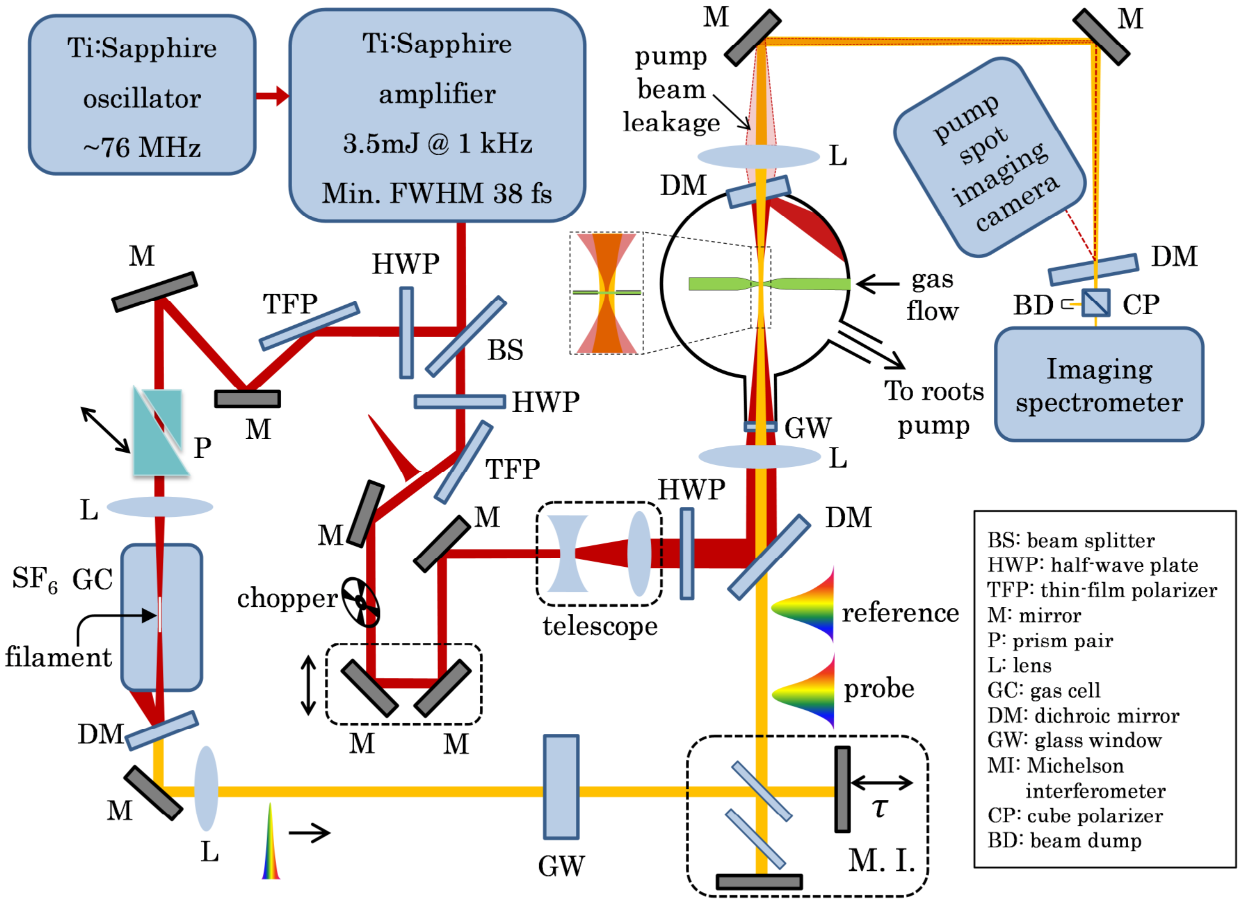

Figure 2.1 The SSSI experimental setup.

The output beam from the laser is split at a beamsplitter (BS), with one arm used to generate SC (probe/reference arm) and the other is used to nonlinearly excite the gas target (pump arm). The pump pulse energy is controlled by a set of half-wave plate (HWP) and thin-film polarizer (TFP).

We employed an optical chopper in the pump arm to obtain signal (pump on) and background (pump off) in close succession (49 shots or milliseconds apart). This method of background collection compensated for any long term drifts in the apparatus, including drifts in the probe and reference spectra employed in spectral interferometry.

The pump beam diameter (FWHM) is expanded from 4 mm to ~10 mm with a telescope for several reasons. First, when a pump pulse with a lower intensity gradient propagates through air and transmissive optics, the nonlinear spatial / temporal phase distortion from self-focusing / self-phase modulation can be mitigated. Second, this can weaken the unwanted phase shift contribution from the focusing lens and the chamber entrance window. Finally, to obtain the whole phase shift caused by the pump beam at the focal point in the transverse direction, this expansion makes $d_{c,probe} >> d_{c,pump}$ (d_c stands for the confocal parameter); therefore, the probe spot size at the focal point is much larger than that of the pump spot.

Another half-wave plate is put in the pump arm to enable the control of the relative pump-probe polarization. This is important for the separation of the instantaneous and rotational responses (detailed in sec. 3.2).

The SC source used in experiments is produced via a single filament generated by a lens with ~f/50 in a half meter long gas cell filled with 2~3 atm sulfur hexafluoride (SF_6) gas. Sapphire windows were used on the cell because they were found to resist etching from the products of dissociated fluorine (such as HF) generated by filamentation. Carefully adjusting the beam diameter and pulse energy makes possible stable, bright and extremely broadband (white) SC pulses. Compared with the SC formerly obtained using conical emission [20], this SC has much less spatial chirp and divergence. The usable bandwidth of the SC is ~200 nm, giving ~5 fs time resolution according to the Fourier transform limit.

It is observed that when the pump pulse duration is minimized at the gas target, in the probe arm, the bright and broadband SC pulses are lost. This is due to the big difference between the dispersions experienced by the pump pulse and the SC excitation pulse. To solve this problem, before the SC generation cell in the probe arm, we use a BK7 glass prism pair to simultaneously minimize the excitation pulse width in the SC cell and the pump pulse width at the chamber gas target. One of the prisms is on a translation stage, and the dispersion difference is therefore controlled by adjusting the amount of glass that the SC excitation pulse passes through. The extra glass compensates for the dispersion in the lenses and windows in the pump path. Additionally, this tunable compensation - helps to keep SC probe optimized when we perform experiments that involve varying the pump pulse duration.

At the output of the gas SC cell, a zero degree dichroic mirror is used to reject the 800 nm excitation beam. Two SC pulse replicas are then generated and temporally separated using a Michelson interferometer.

The SC and pump pulses are combined with a 45 degree dichroic mirror, and then co-propagate. They are focused onto a *thin* gas flow target (detailed in sec. 2.3) by a lens with focal length ~40 cm, and then the pump is rejected with another dichroic mirror, which is also the exit window of the chamber. The refractive index disturbance imparted to the gas by the pump pulse is encoded on the probe pulse, and manifest as a wavelength-dependent phase shift. The laser-gas interaction region in the thin flow target is imaged with an achromatic lens onto the entrance slit of an imaging spectrometer. The spectrometer relays the image of the slit, spectrally dispersed, to a CCD camera. The probe and reference SC pulses interfere in the spectral domain inside the spectrometer, with the wavelength-dependent interference pattern (the spectral interferogram) recorded on the CCD at the spectrometer image plane. The 2D spectral interferogram is space resolved along the fringes and wavelength resolved perpendicular to them. The effect of the pump is a space-resolved and wavelength-dependent fringe shift. It is this fringe shift that is analyzed for extracting the refractive index transient.

Practically, it's found that performing a multi-shot averaging of interferograms *before* phase extraction can enhance the signal-to-noise ratio, which is proportional to $\sqrt{N_{int}}$, where N_{int} is the number of averaged interferograms [20, 21]. This averaging not only reduces a significant amount of data processing time but enables measuring a phase shift smaller than the noise level. One should note that compared with the conventional multi-shot techniques that typically rely on the scan of the pump-probe delay to get time-resolved information, SSSI is still classified as a single-shot technique, even with the aid of the multi-shot averaging, because the material temporal nonlinearity information (within ~2 ps) can be acquired in one shot.

In addition, since the pump beam pointing may drift over time, it is required to monitor it to assure the probe beam entering the spectrometer give the strongest signal. To do this pump spot imaging, right before the spectrometer we use one more dichroic mirror with high reflectivity at 800 nm and a CCD camera to capture the pump beam leakage from the chamber exit window.

2.3 The importance of using a thin gas target

A well-defined interaction length L_{eff}, ideally much shorter than the confocal parameter of the pump $d_{c,pump}$, minimizes spatial and temporal distortions due to axial variation in the pump intensity [56]. This is also of great importance while performing ionization rate measurements, as a plasma can refract the probe beam (effectively negative lensing).

We note that experiments with $L_{\text{eff}} \gg d_{c,pump}$, which is the case for most gas cells [9, 10, 20, 21], suffer from two main problems: (i) the three-dimensional pump and probe beam profiles are imprecisely known, and (ii) even if known, nonlinear pump propagation would distort them. In any case, the probe will pick up a complicated mixed space-time perturbation.

In our experiment, the interaction takes place in a very thin gas flow of effective thickness $L_{\text{eff}} \ll d_{c,pump}$ [4, 48]. Therefore, the pump intensity is axially uniform along the interaction length.

If not specified, the gas flow target consists of a stainless steel tube with 90-μm-thick walls. The central section of the tube is pinched and 80-μm-diameter entrance and exit holes are laser drilled through it. The gas leak through the small holes (mass flow rate) is then limited by their sizes. With an input flow pressure of 1 atm in the tube, the background pressure in the chamber is about 200 mTorr.

2.4 Phase reconstruction

In the time domain, the perturbed (pump on) probe field $\bar{E}_{probe}(x,t)$ can be expressed as an unperturbed (pump off) probe $E_{probe}(x,t)$ multiplied by a phase shift $e^{i\Delta\Phi(x,t)}$:

$$\bar{E}_{probe}(x,t) = e^{i\Delta\Phi(x,t)} E_{probe}(x,t) \tag{2}$$

Fringes in SSSI spectral interferograms give not only the spectral phase shift $\Delta\varphi(x,\omega)$, but the spectral amplitude $\left|\bar{E}_{probe}(x,\omega)\right|$ and $\left|E_{probe}(x,\omega)\right|$. The time domain phase shift $\Delta\Phi(x,t)$ can be reconstructed, using equation 2, as [56]:

$$\Delta\Phi(x,t) = Im\left\{\ln\left[\frac{\int\left|\bar{E}_{probe}(x,\omega)\right|e^{i\varphi_S(\omega)+i\Delta\varphi(x,\omega)}e^{i\omega t}d\omega}{\int\left|E_{probe}(x,\omega)\right|e^{i\varphi_S(\omega)}e^{i\omega t}d\omega}\right]\right\} \tag{3}$$

Here $\varphi_s(\omega)$ is the spectral phase of the probe without the pump on, determined by both the SC pulse stretching and details of the SC generation. $\varphi_s(\omega)$ is typically dominated by second order dispersion, which implies an almost linear mapping between ω and time t. It can thus be written in the simple form, $\varphi_s(\omega) = \mathrm{GDD}\cdot(\omega-\omega_0)^2$, where GDD is group delay dispersion and ω_0 is an arbitrary (typically central probe) frequency. By scanning the pump-probe delay, the GDD can be measured by performing a linear fit for the spectral positions where pump and probe pulses overlap with each other.

2.5 Folded wavefront interferometry

Folded wavefront interferometry is another technique we use in the experiments described in this thesis [57, 58]. A folded wavefront interferometer is composed of two beamsplitters and several routing mirrors. The incoming beam is divided into two by the first beamsplitter. These two beams are routed by metal mirrors separately and then recombined with the second beamsplitter. The relative crossing angle between the two beams is adjusted to give the desired fringe spacing of the interferogram recorded with the CCD camera. Well-known fringe analysis techniques are described in [58].

Chapter 3

Absolute measurement of optical nonlinear refractive index (n_2) and polarizability anisotropy ($\Delta\alpha$) in diatomic molecular gases

3.1 Introduction

In this chapter, we present absolute measurements of the optical nonlinearity in O_2, N_2, N_2O, Ar, H_2 and D_2. Our method can be extended to most transparent media provided the sample is thin enough. Here, we determine accurate values of the instantaneous Kerr coefficient n_2 and the molecular polarizability asymmetry $\Delta\alpha = \alpha_{\parallel} - \alpha_{\perp}$, where $\alpha_{\parallel}$ and $\alpha_{\perp}$ are the linear polarizabilities along and across the molecular bond axis.

In all of the gases studied here, the first ionization potential is far above the laser photon energy of 1.55 eV. As a result, the nonlinear response of the electronic states is essentially instantaneous and is characterized in terms of the Kerr coefficient n_2. In addition, molecular gases can have an important, even dominant, response due to the alignment and stretching of the molecular bonds in the intense laser field [7, 9, 59]. This response can be described by a time-domain Raman response function $R(t)$. The total nonlinear index of refraction, to second order in the field or first order in the laser intensity, is given by the Eq. 1.1: $\Delta n(t) = n_2 I(t) + \int_{-\infty}^{t} R(t-t')I(t')dt'$, where $I(t)$ is the laser intensity.

The orientational (bond stretch and molecular alignment) contribution to the instantaneous electronic response is fourth order in the field amplitude and is negligible on the time scale of the $n_2 I(t)$ response [21]. In the gases studied here, the small adiabatic bond stretch contribution to $R(t)$ cannot be separated out because the spacing between vibrational states is much greater than the bandwidth corresponding to our 40-fs (FWHM) pump pulse. At high intensity, there is an additional contribution from free electrons generated by ionization [48], but for all data presented later, the intensity is kept below the ionization threshold.

3.2 Determination of the effective interaction length

To measure the values of n_2 and $\Delta\alpha$ with quantitative accuracy, one must know the effective interaction length in the thin gas target L_{eff}. Because the measured probe phase shift in the tube depends on the local pressure, the definition of L_{eff} is given as [4]

$$\Delta\Phi(x,t) = k_0 \int \Delta n(x,z,t)dz = k_0 \Delta n_{atm}(x,t) \int \frac{P(z)}{P_0} dz = k_0 \Delta n_{atm}(x,t) L_{\text{eff}} \tag{4}$$

where x is the transverse coordinate in the sample, z is the axial coordinate along the interaction region, k_0 is the average vacuum wavenumber of the chirped probe pulse over the frequency range it overlaps with the pump pulse, $P(z)$ is the pressure distribution, and $\Delta n_{atm}(x,t)$ is the change in refractive index at atmospheric pressure P_0.

A folded wave-front interferometer employing a 635-nm cw diode laser was used to measure L_{eff} in the flow tube. The portion of the beam passing through the laser-drilled hole interfered with light passing outside the tube, and the hole was imaged to a CCD camera as shown in Fig. 3.1. Interferograms were captured at a frame rate of 14.5 s^{-1} as the gas flow into the tube is suddenly shut off. The difference in phase between the initial state of steady flow and long times after shut off, when the tube is evacuated, can be expressed as $\Delta\varphi = k_0(n_0 - 1)L_{\mathrm{eff}}$, where n_0 is the refractive index at 1 atm. Measuring $\Delta\varphi$ = 1.16 rad and using $n_0 - 1$ = 2.795×10^{-4} for 633 nm in N_2 at 1 atm [20], we find L_{eff} = 418 μm. Using this value for L_{eff} with our spectral interferometry phase shifts gives absolute values of Kerr nonlinearity at 1 atm. (Since the outer thickness of the tube is 475 μm, this implies an average pressure inside the tube of slightly less than 1 atm.)

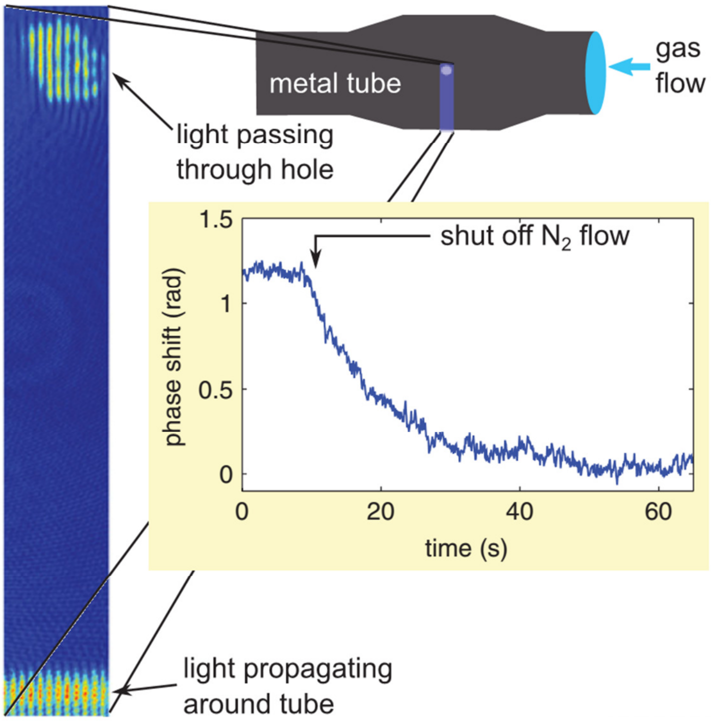

Figure 3.1 Measurement of the linear phase shift due to the gas in the thin tube, measured using folded wavefront interferometry. The inset shows a schematic of the flow tube and an example interferogram.

3.3 Separation of instantaneous nonlinear response and delayed rotational response in diatomic molecular gases

As shown in Eq. 1.1, the response is composed of instantaneous and rotational parts. To separate these contributions, we recognize that if $\Delta\Phi_{\parallel} = \Delta\Phi_{inst} + \Delta\Phi_{rot}$ for probe polarization parallel to the pump, then symmetry properties of the nonlinear susceptibility tensor [60] imply $\Delta\Phi_{\perp} = \frac{1}{3}\Delta\Phi_{inst} - \frac{1}{2}\Delta\Phi_{rot}$ for probe polarized perpendicular to pump. These equations yield

$$\Delta\Phi_{inst} = \frac{3}{5}(\Delta\Phi_{\parallel} + 2\Delta\Phi_{\perp}) \tag{3.1}$$

and

$$\Delta\Phi_{rot} = \frac{2}{5}(\Delta\Phi_{\parallel} - 3\Delta\Phi_{\perp}). \quad (3.2)$$

These are shown in Fig. 3.2 as red dotted $(\Delta\Phi_{inst})$ and green dash-dotted $(\Delta\Phi_{rot})$ lines. The instantaneous response is proportional to the temporal shape of the pulse $I(t)$, and the small bump at early time delays has been verified as a real feature of the laser pulse using spectral phase interferometry for direct electric-field reconstruction [61].

We average 1000 interferograms before performing the extraction [20], allowing measurement of phase shifts smaller than possible in a single shot. The dominant source of noise in a single-shot measurement is CCD pixel noise.

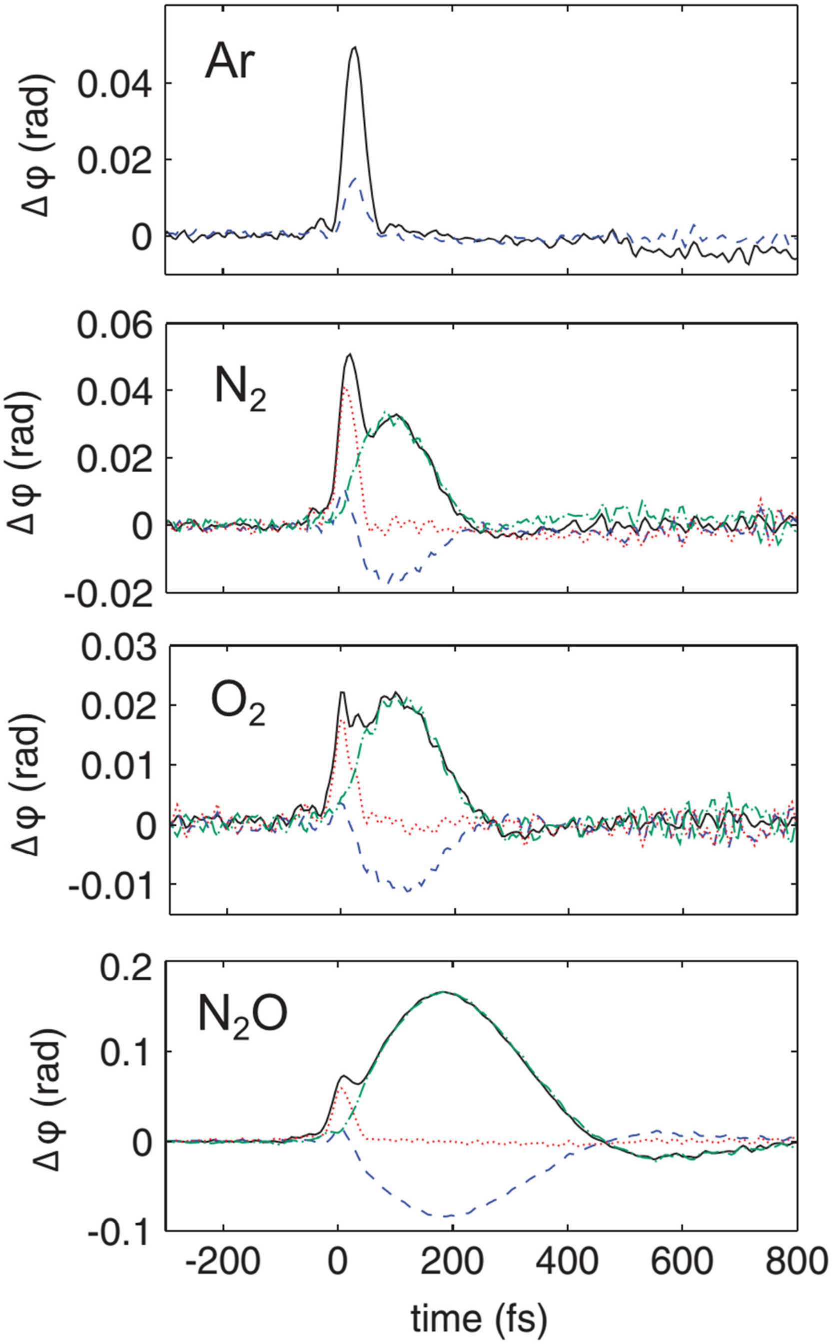

Figure 3.2 Lineouts showing the phase shift $\Delta\Phi(t)$ for pump polarization parallel to probe (solid black line) and pump perpendicular to probe (blue dashed line). Also shown is the decomposition of the signal into the instantaneous (red dotted line) and rotational (green dash-dotted line) signals, as described in the text. The pressure used for each gas was 90 Torr. The peak intensity used for each gas was Ar, 41 TW/cm^2; N_2, 45 TW/cm^2; O_2, 14 TW/cm^2; and N_2O, 28 TW/cm^2.

3.4 Determination of n_2 and $\Delta\alpha$: results and discussion for N_2, O_2, Ar and N_2O

To measure the spatial distribution of the pump intensity without relying on external imaging of the focal spot, we measure the instantaneous Kerr phase shift along two perpendicular slices $\Delta\Phi(x,t)$ and $\Delta\Phi(y,t)$, using a Dove prism rotated 45 degrees around the longitudinal axis to rotate the image on the spectrometer slit by 90 degrees. We find that the pump spot size at the target is 29 μm × 27 μm. This is shown in Figs. 3.3(a) and 3.3(b). The beam profile measured is used to find the relation between the pulse fluence and the peak intensity.

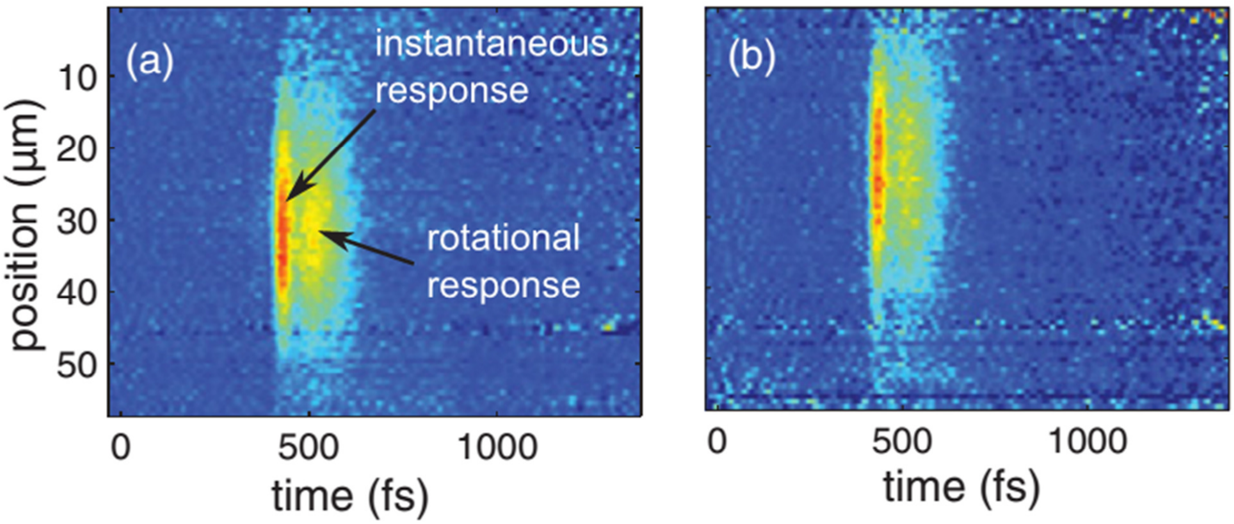

Figure 3.3 Measurement of absolute phase shifts in N_2 using a 475-μm-thick gas target with L_{eff} = 418 μm. (a, b) Nonlinear phase shift extracted using SSSI at peak laser intensity 41 TW/cm^2 along two perpendicular slices x and y through the probe spot.

Consequently, n_2 can be calculated from the peak nonlinear phase shift $\Delta\Phi_{inst,peak} = 2 \times 2\pi(n_2 I_{peak})L_{\mathrm{eff}}/\lambda_{c,probe}$, where $\lambda_{c,probe}$ is the central probe frequency of where the pump overlaps with the probe. Note that we added an additional factor of 2 because when the pump and probe beams are distinguishable, the nonlinear phase shift we got from this cross-phase modulation measurement would be double of that from a self-phase modulation measurement [51].

We attribute the instantaneous phase shift to the electronic response because the adiabatic bond stretch contribution is small: using the rovibrational response function plotted in [59] to simulate the instantaneous phase shift due to adiabatic bond stretching in N_2 and O_2 gives a result ~30 times smaller than our measured instantaneous phase shift. This is consistent with Shelton and Rice [12], who showed that neglecting the vibrational component of the Kerr effect results in errors in the nonlinear susceptibility of less than 10%.

With an absolute measurement of nonlinearity in N_2 from the thin gas flow, we can perform relative phase-shift measurements in all other gases with the vacuum chamber backfilled at low pressure (here ~90 Torr) and reference the phase shifts to the flow-tube measurement, allowing a higher signal-to-noise ratio. There was no measurable phase front distortion of the pump due to self-focusing (peak power is ~1% of critical at 90 Torr). Lineouts of the phase shift measured for each gas for pump parallel (black solid line) and perpendicular (blue dashed line) to probe are shown in Fig. 3.2. Scaling the N_2 backfill data to match the flow tube data, we find an effective interaction length at 90 Torr of 4.41 mm, which is used for the rest of the gases.

We fit the delayed response to the second term in Eq. 1.1. The rotational part of $R(t)$ is proportional to the ensemble average molecular alignment $\langle\cos^2\theta\rangle - 1/3$ calculated using a density matrix code [62], where θ is the angle between the molecular axis and the optical field direction. The only inputs to the code are $\Delta\alpha$ and the molecular moment of inertia, where the latter is known to high accuracy from rotational spectroscopy [23]. We find the values of $\Delta\alpha$ from the simulations that best match experiment. [There is no delayed vibrational response contributing to $R(t)$ because the bandwidth of the pump pulse is not sufficient to excite vibrational modes.]

Our results are summarized in Table 1. The largest source of uncertainty is the peak intensity, which depends on the laser spot size, average power, and pulse width. The error is reduced by employing the full transverse profile of the intensity as measured in Figs. 3.3(a) and 3.3(b), for example. Note that the uncertainty values given in Table 1 are the absolute error; the relative contribution between n_2 and $\Delta\alpha$ was measured much more precisely because it does not depend on the peak intensity. Ratios of values between gases are also more precise than the absolute error given because the focusing conditions were identical.

Table 1 The measured Kerr coefficient n_2, polarizability anisotropy $\Delta\alpha$, and the ratio of the effective n_2 values for a short pulse to a long pulse for each gas studied and a comparison with previous experimental and theoretical work.

	n_2 (10^{-20} cm^2/W)				$\Delta\alpha$ (10^{-25} cm^3)			$n_2/n_{2,long}$
Gas	This work	Nibbering *et al.* [7]	Loriot *et al.* [10, 11]	Shelton & Rice [12]	This work	Lin *et al.* [63]	Bridge *et al.* [18]	This work
Ar	9.7±1.2	14±2	10.0±0.9	10.4				
N_2	7.4±0.9	23±3	11±2	8.1	6.7±0.3	9.3	6.96	0.23
O_2	9.5±1.2	51±7	16.0±3.5	8.7	10.2±0.4	11.4	10.99	0.14
N_2O	17.2±2.2				28.1±1.1	27.9	29.6	0.04

In the limit of a long pulse, the rotational response is adiabatic, and the effective instantaneous Kerr coefficient has both electronic and rotational components. One can show using a perturbative calculation [21] that

$$n_{2,long} = n_2 - \frac{4\pi N(\Delta\alpha)^2}{15 n_0^2 c^2 \hbar B} \times \left[\sum_j \frac{j(j-1)}{(2j-1)^2} \left(\frac{{\rho_j}^{(0)}}{2j+1} - \frac{{\rho_{j-2}}^{(0)}}{2j-3} \right) \right]$$

where N is the gas density, B is the rotational constant, and

$${\rho_j}^{(0)} = \frac{D_j(2j+1)e^{-hcBj(j+1)/k_B T}}{\sum_k D_k(2k+1)e^{-hcBk(k+1)/k_B T}}$$

where k_B is Boltzmann's constant, T is the gas temperature, and D_j is a statistical weighting factor that depends on nuclear spin. The ratio of n_2 to $n_{2,long}$ for each gas at atmospheric density and room temperature, calculated from our measured values of n_2 and $\Delta\alpha$, is also shown in Table 1. We use B = 2.0 cm^{-1} for N_2, B = 1.44 cm^{-1} for O_2, and B = 0.41 cm^{-1} for N_2O [63].

Previous measurements of n_2 in the gases studied here varied widely [7, 9-11], in part because ~100-fs pulses were used, and thus the instantaneous response was difficult to separate reliably from the rotational response. In addition, several techniques [7, 8] depend sensitively on three-dimensional nonlinear propagation effects. In general, a possible source of error in pump-probe measurements arises from using degenerate pump and probe pulses. This can lead to spurious results from two-beam coupling through an intensity or plasma grating [50]. For instance, the given n_2 values for N_2 and O_2 in [10, 11] are corrected with the nonlinear rotational grating theory [51]. After the correction, our measurements agree within their uncertainty estimates. In contrast, due to lack of rotational response, the n_2 values of Ar are already within the uncertainty range of each other [10, 11, 51].

Possible dispersion in the nonlinear susceptibility was addressed by simply changing the pump-probe time delay. This varied the supercontinuum (SC) probe wavelength band temporally overlapping the pump. There was no measurable variation, to within error, in n_2 or $\Delta\alpha$ over the central probe wavelength range of 550–635 nm for any of the gases studied. This is consistent with dispersion estimates using a power series expression [12, 64], showing that for a SC probe at a central wavelength of 580 nm, we overestimate n_2 at 800 nm by less than 3%, smaller than our error bars.

It is interesting to consider how the electronic response merges with the rotational as the pump pulse duration increases. Previously, the pulse-width dependence of the Kerr effect had been probed only indirectly by measurements of critical power in self-focusing [59, 65]. However, it was recently shown that critical power measurements can be complicated by defocusing effects from plasma generation [66]. Figure 3.4 shows the pump–pulse-width–dependent response of N_2, with the pump energy kept constant. For clarity, the curves are horizontally shifted. It is seen that for pulses longer than ~80 fs, the instantaneous response merges with the rotational. This is consistent with prior work with ~100-fs pulses [20, 21, 23] and applies to the vast majority of filamentation experiments in air [2]. The results of Fig. 3.4 also allow us to test the validity of Eq. 1.1, whose curves are overlaid on the experimental curves. The experimental results are in good agreement with the simulations.

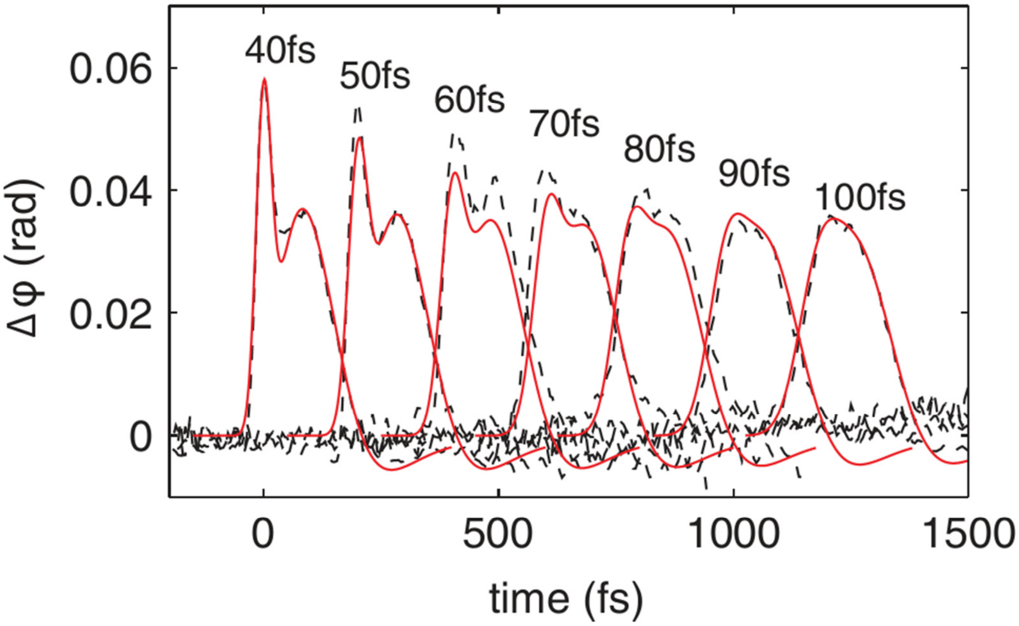

Figure 3.4 Pulse-width dependence of the nonlinear response in N_2. Measured phase shift extracted using SSSI (black dashed line), with the pulse width varied between 40 and 100 fs by adjusting the compressor. The pulse energy is kept constant. Also shown is the phase shift calculated (red solid line) using Eq. 1.1 and the parameters (n_2, $\Delta\alpha$) measured with a 40-fs pulse.

3.5 Results and Discussion for H_2 and D_2

H_2 and D_2 have large rotational constants B (small moments of inertia), hence a bigger energy spacing ($\propto hcB$) between rotational states and fewer states are populated at a given temperature. The quarter revival period of H_2 and D_2 are ~70 and 143 fs (compared to ~2.1 / 2.9 ps for N_2 / O_2, respectively).

Figure 3.5 and 3.6 show two dimensional SSSI space-time phase maps for ~0.3 atm chamber-backfilled H_2 and D_2 at ~46 TW/cm^2, including the cases of parallel ($\mathbf{E}_{pump} \parallel \mathbf{E}_{probe}$) and perpendicular polarization ($\mathbf{E}_{pump} \perp \mathbf{E}_{probe}$). The pump pulse durations are 40 and 50 fs for H_2 and D_2, respectively. In H_2, we speculate that the negative response right after time zero is caused by the molecular vibrational response. This question will be pursued in future work.

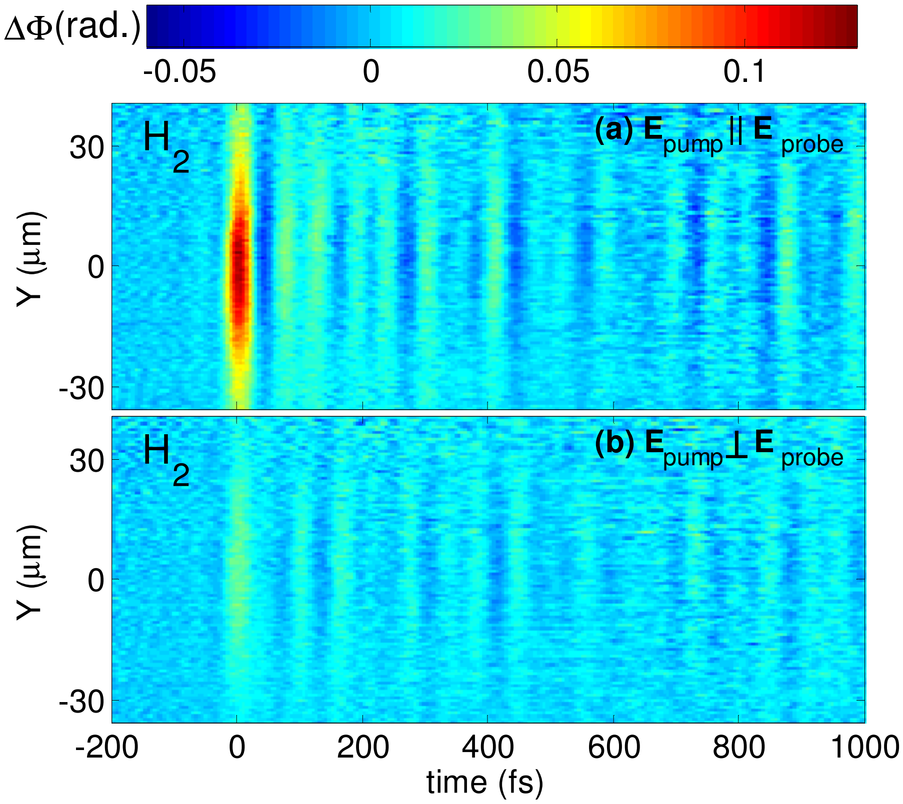

Figure 3.5 Example 2-D phase maps for H_2 when (a) $\mathbf{E}_{pump} \parallel \mathbf{E}_{probe}$ and (b) $\mathbf{E}_{pump} \perp \mathbf{E}_{probe}$.

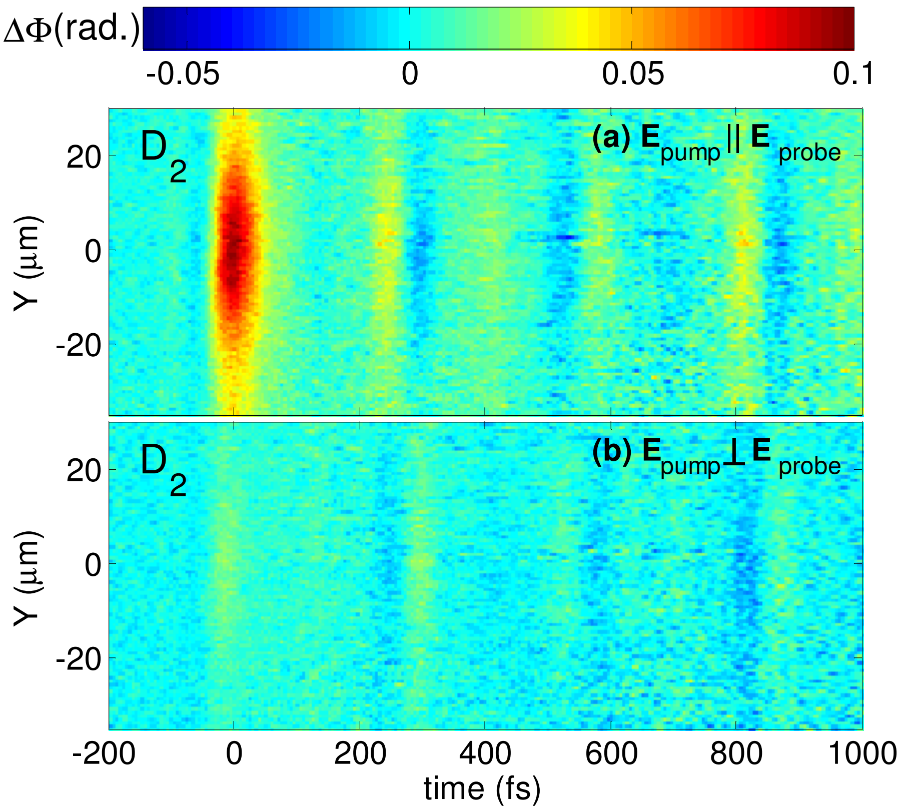

Figure 3.6 Example 2-D phase maps for D_2 when (a) $\mathbf{E}_{pump} \parallel \mathbf{E}_{probe}$ and (b) $\mathbf{E}_{pump} \perp \mathbf{E}_{probe}$.

The instantaneous and rotational responses for H_2 and D_2 are separated with Eq. 3.1 and 3.2, and the corresponding lineouts are shown in Fig. 3.7.

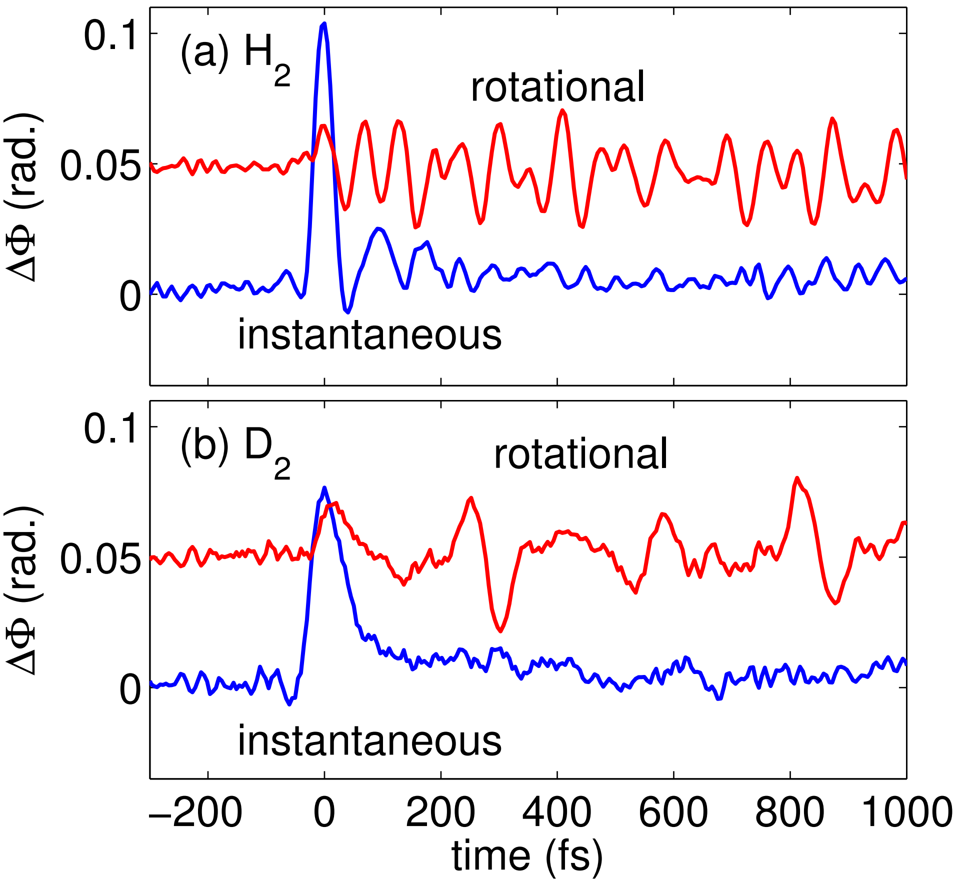

Figure 3.7 Lineouts of instantaneous and rotational responses of (a) H_2 and (b) D_2.

Compared with N_2, O_2 and N_2O, clearly in H_2 and D_2 we observed finer transient oscillations, resulting from the quantization of fewer available rotational levels compared to say N_2 or O_2.

To see how the rotational responses of H_2 and D_2 vary with pump pulse width at a fixed energy, we did a series of calculations and SSSI measurements. Figure 3.8 shows density matrix calculation results and the experimental SSSI data at ~0.3 atm with the pulse energy fixed at 34 μJ. The intensities range from 22 to 54 TW/cm^2.

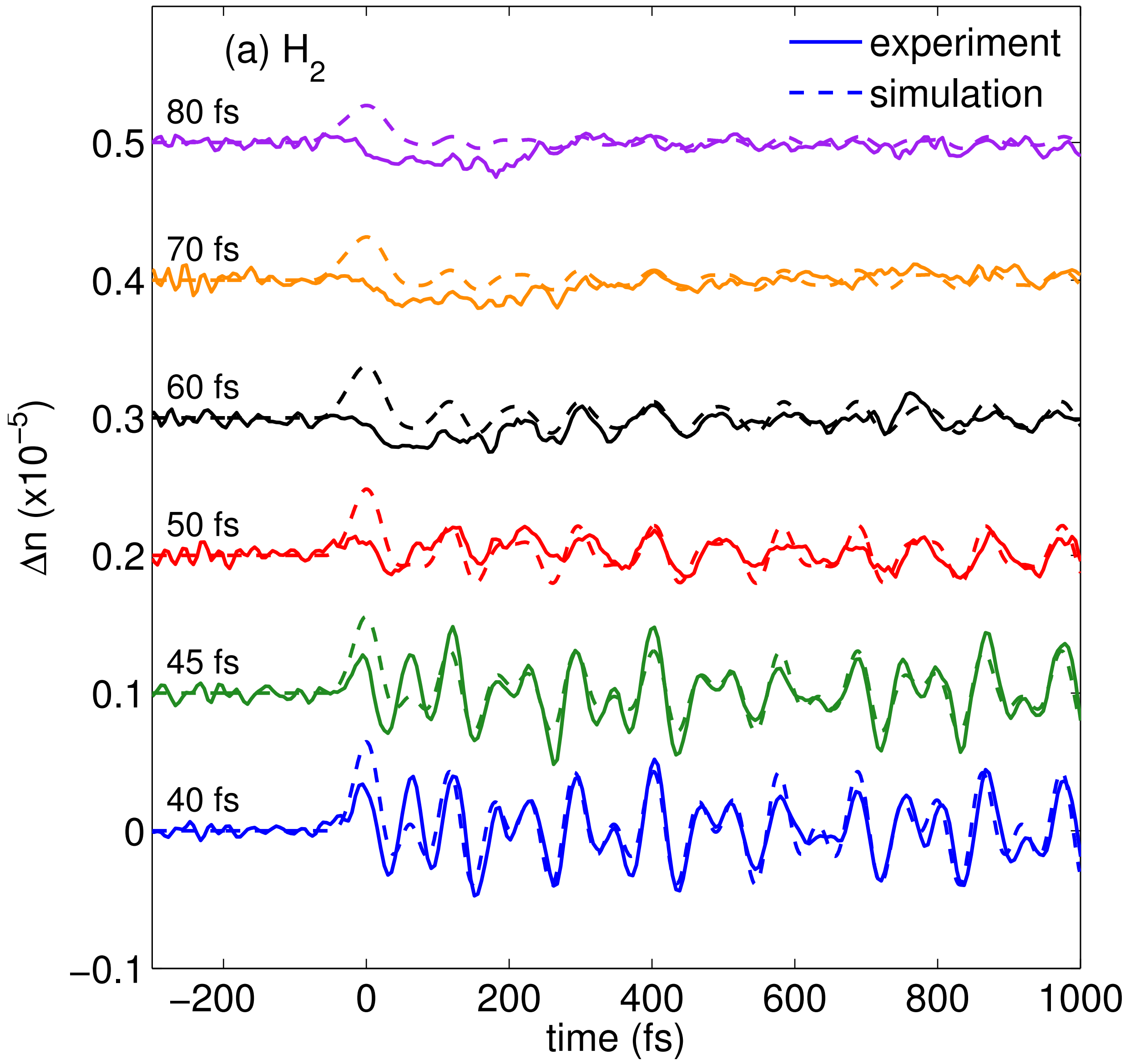
(a) H_2
experiment
simulation
80 fs
70 fs
60 fs
50 fs
45 fs
40 fs
Δn (x10^{-5})
0.5
0.4
0.3
0.2
0.1
0
−0.1
−200
0
200
400
600
800
1000
time (fs)

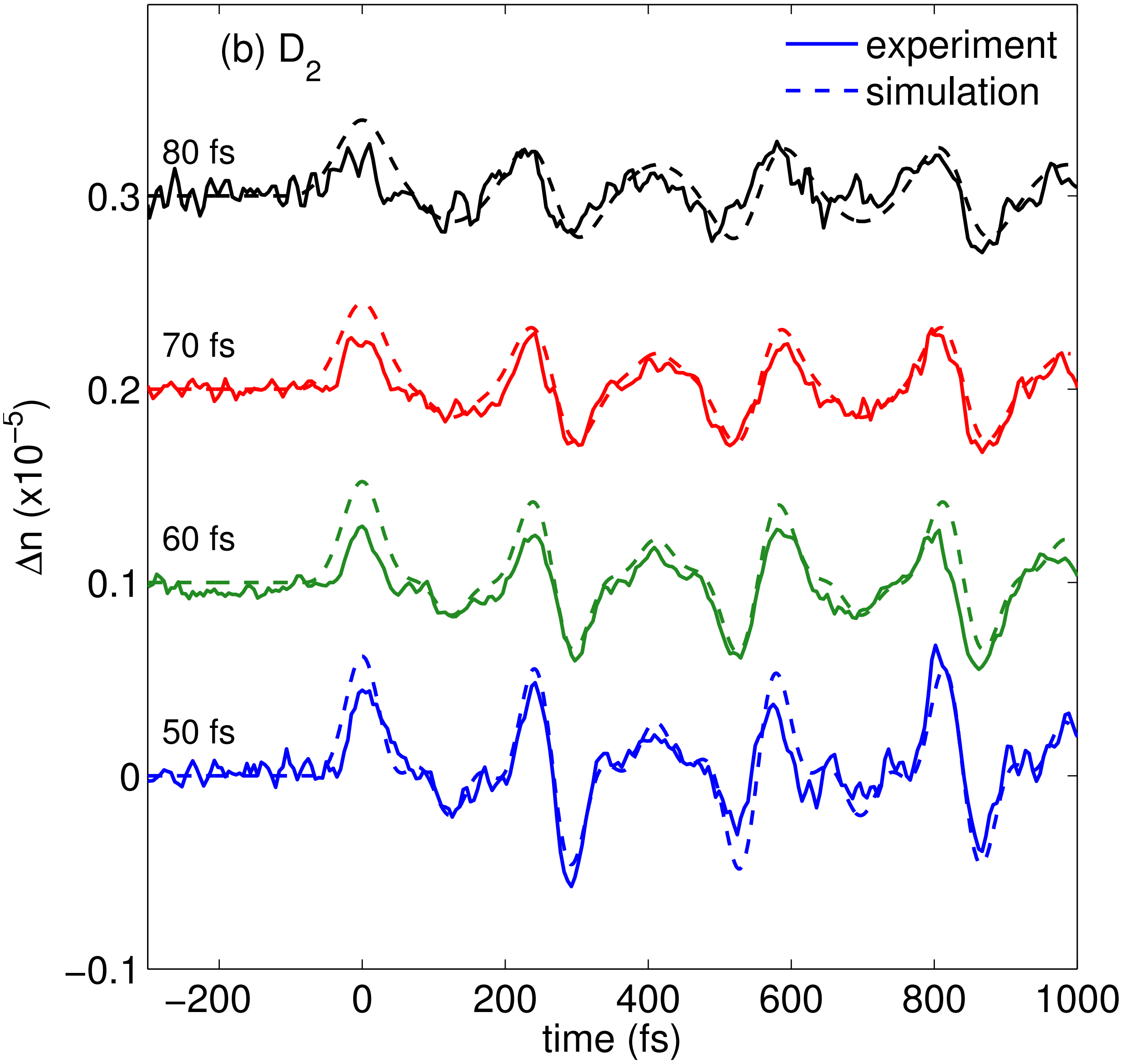

Figure 3.8 Density matrix calculation results and SSSI lineouts of the rotational refractive index change for (a) H_2 and (b) D_2 with pulse width dependence ranging from 40 / 50 to 80 fs.

In Fig. 3.8, it is seen that when the gas is excited with a short pulse (40 fs), the fine structure signatures of rotational revivals can be clearly distinguished; however, their sharp temporal features are reduced for longer pulses, as seen in the density matrix calculation and in previous long-pulse experiments in H_2 and D_2 [21]. The 'smoothing' of the response is due to the reduced effective bandwidth which means fewer exited rotational states [21]. In the shortest pulse case, the results show that the SSSI technique, with its excellent time resolution, is able to resolve all the oscillatory features.

To determine instantaneous n_2 for H_2 and D_2, we used Ar as a reference and measured the ratios of peak instantaneous responses in a backfilled chamber at ~90 Torr with 40 fs pulses. We obtained $\Delta\alpha$ by means of fitting density matrix calculations to the experiment results. The literature values and our results are tabulated in Table 2.

Table 2 Comparison of nonlinear refractive index and polarizability anisotropy of H_2 and D_2.

	n_2 (10^{-20} cm^2/W)		$\Delta\alpha$ (10^{-25} cm^3)		
Gas	This work	Shelton and Rice [12]	This work	Bridge and Buckingham [18]	MacAdam and Ramsey [67]
H_2	6.8±0.9	6.36	3.60±0.14	3.14	3.02
D_2	5.9±0.7	6.19	3.25±0.13	2.99	2.92

The rotational frequency of the rotational state j is $\omega_j = 2\pi c[Bj(j+1) - Dj^2(j+1)^2]$, where D is the centrifugal constant, thus the coupled $\Delta j = 2$ states in a two-photon nonresonant Raman excitation process [21] have a frequency spacing

$$\omega_{j,j-2} = 4\pi c[B(2j-1) - 2D(2j^3 - 3j^2 + 3j - 1)]. \tag{3.3}$$

By taking the Fourier transform of the time resolved rotational response (excited by 40 fs pump pulse at 30 TW/cm^2, data not shown above), we were able to identify the rotational states and frequencies that contribute to molecular alignment: ω_{20} and ω_{31} for H_2; ω_{20}, ω_{31} and ω_{42} for D_2, as shown in Fig. 3.9.

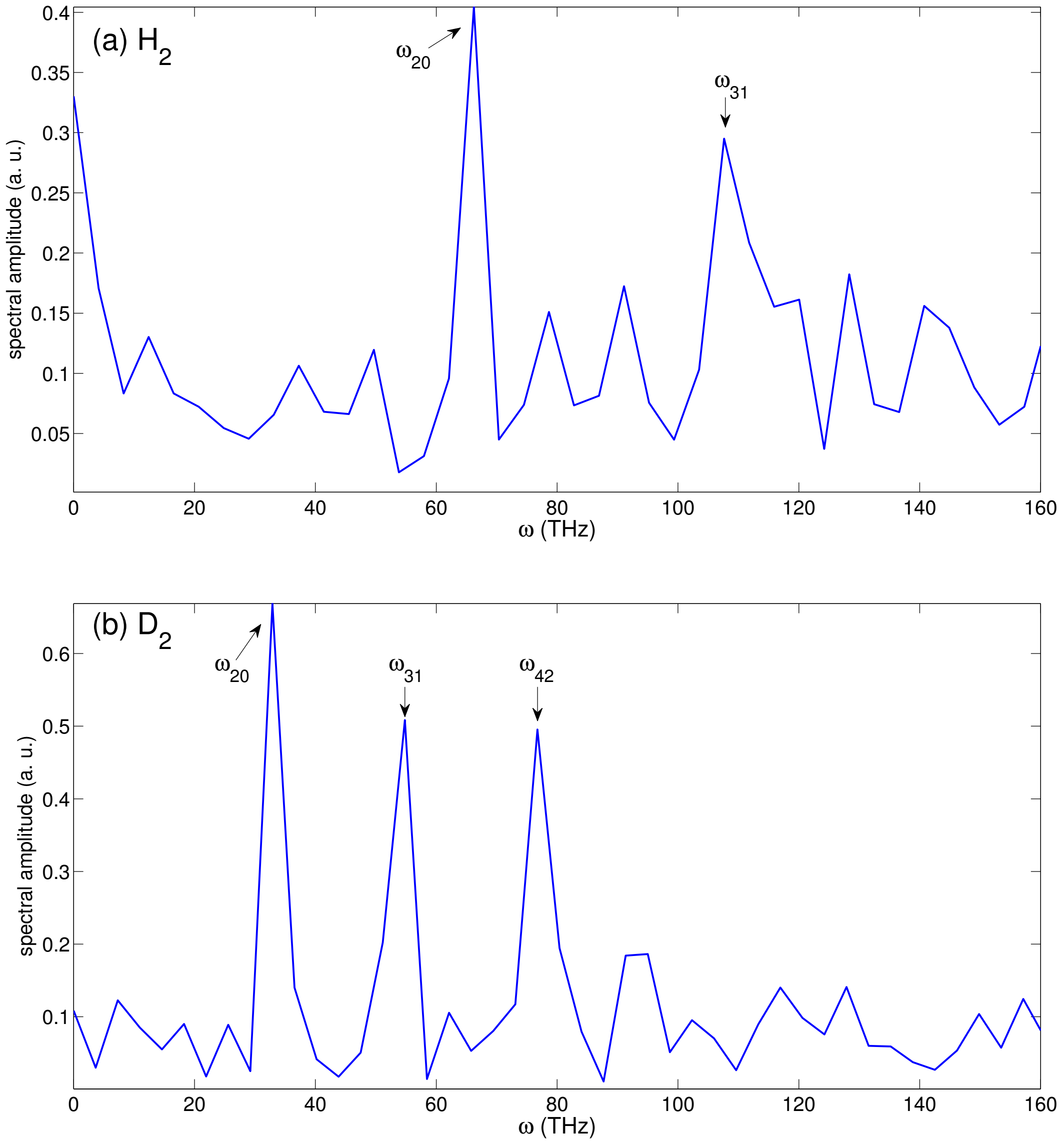

Figure 3.9 The spectra of the time resolved rotational responses of (a) H_2 and (b) D_2.

For H_2, after solving Eq. 3.3 with ω_{20} and ω_{31}, we got B_{H_2}= 59.4 cm^{-1} and D_{H_2}= 0.2 cm^{-1}; for D_2, through performing a least square fit to Eq. 3.3 with ω_{20}, ω_{31} and ω_{42} we got B_{D_2}= 29.1 cm^{-1} and D_{D_2}= 0 cm^{-1}. A comparison with literature values is given in Table 3. The uncertainty is estimated by the grid spacing of the spectrum.

Table 3 Comparison of the rotational and centrifugal constants of H_2 and D_2.

rotational constant B (cm^{-1})			
Gas	This work	Chen *et al.* [21]	NIST [68]
H_2	59.4±2.4	61.8	60.853
D_2	29.1±1.1	30.4	30.443

centrifugal constant D (cm^{-1})		
Gas	This work	NIST [68]
H_2	0.2 ± 0.1	0.0471
D_2	0	0.01141

3.6 Conclusion

In summary, we have presented direct measurements of the optical nonlinearity in the major components of air, H_2, D_2 and N_2O using supercontinuum spectral interferometry. Our measurements indicate that the instantaneous response in these gases was overestimated in previous experiments that directly measured the Kerr coefficient, probably because of the use of longer pulses. Our measurements agree to within error with previous experiments that use harmonic generation and a theoretical model for the dispersion of the third-order susceptibility [12]. Our results should significantly improve simulations of pulse compression and filamentation in these gases, with special application to atmospheric propagation.

Chapter 4

Optical nonlinearity near the ionization threshold

4.1 Direct measurement of gas nonlinearity in Ar and N_2

Loriot *et al.* used a nonspatially resolved multishot technique limited in time resolution by the probe duration of ~90 fs [10]. They measured the transient birefringence and inferred the higher-order Kerr coefficients from the tensorial symmetry of the nonlinear susceptibilities, $\chi^{(5)}$, $\chi^{(7)}$, etc. [10, 69]. In contrast, we can measure parallel and perpendicular components of the nonlinear response independently.

Previously, supercontinuum spectral interferometry was used with 110 fs pump pulses to study the nonlinear response of air constituents [20], and no sign reversal of the nonlinear index was observed up to intensities where ionization occurs. However, the use of a gas cell complicates the interpretation of the experiment when the response is highly nonlinear [56]. Also, at the high pressures used (> 3 atm), plasma-induced refraction limits the peak intensity. Here, we measure the nonlinear response of Ar and N_2 by using a 38 fs pump pulse and a 2 mm thick gas target.

The SSSI experimental setup is as shown in Fig. 2.1. Roughly 700 μJ of the laser output is used to generate supercontinuum covering 640–720 nm in a gas cell filled with 1–2 atm of Ar; the fundamental is rejected by a dichroic mirror. The supercontinuum is linearly polarized. Probe and reference pulses, separated by 1.4 ps, are generated with a Michelson interferometer and chirped so that the group delay dispersion is 1950 fs^2, and then the beam is spatially filtered with a 100 μm pinhole. The pump and supercontinuum are combined by a dichroic mirror; at this point the pump beam is about 5 times wider than the probe or reference beam so that the probe spot overfills the pump spot in the interaction region.

The pump and probe beams are focused by a lens of focal length 40 cm and enter the vacuum chamber through a 5 mm thick fused silica window, propagating 30 cm through vacuum to the target. The pump beam waist, measured by imaging the focus onto a CCD camera, is 22 μm FWHM.

The target is a copper gas flow tube with a flattened section through which a 120 μm diameter hole was laser drilled to allow the pump and probe to pass through. The space between the inner tube walls is 1 mm, with a wall thickness of 0.5 mm. A roots pump keeps the background pressure of the chamber at 400 mTorr, and the local gas density drops quickly enough away from the tube that the probe phase shift is dominated by the gas between the holes.

The pump pulse, centered at time $t = t_{pump}$ and transverse dimension $x = x_{pump}$, induces a phase shift in the probe pulse $\Delta\phi(x,t)$. In the data shown here, we have subtracted a very small background signal due to cross phase modulation in the entrance window. An example extracted time domain phase shift $\Delta\phi(x,t)$ of the probe for Ar at 60 TW/cm^2 pump vacuum intensity is shown in Fig. 4.1(a). The time resolution is given by the probe bandwidth (in this experiment 15 fs), and the transverse spatial resolution is 3 μm. The intensity values given here are calculated from the pulse duration, the average power, and the measured beam profile—we estimate an uncertainty of 20%. The signal-to-noise ratio is considerably improved by summing multiple interferograms before performing the phase extraction [20]; in all of the data presented here, 300 interferograms were summed at each power and polarization.

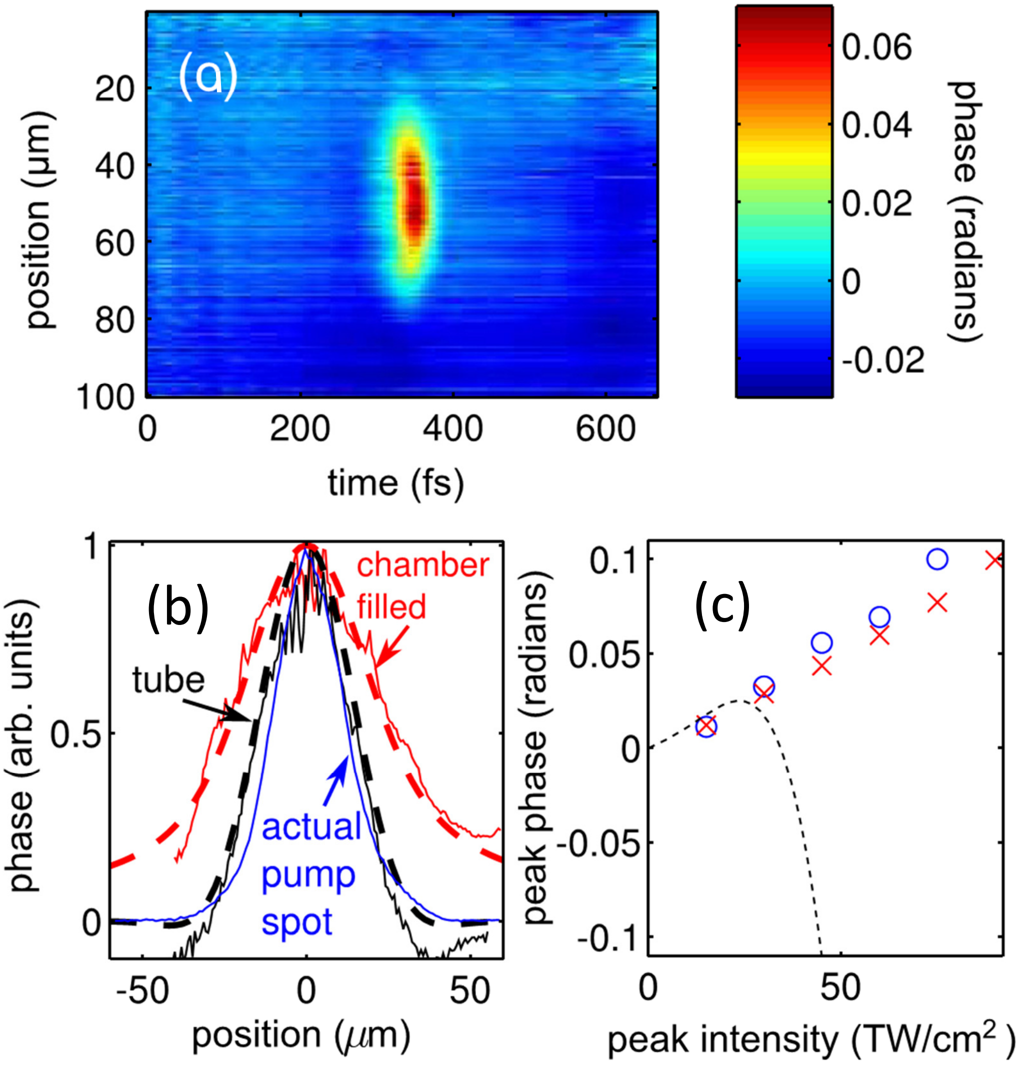

Figure 4.1 Experimental results. (a) Map of phase versus time and transverse dimension for Ar at $I_{peak} = 60$ TW/cm^2, extracted as described in Ref. [19]. (b) Lineout of the pump spot, comparing the signal using the drilled flow tube to the signal with a backfilled chamber. The true pump spot is also shown for comparison. The dashed lines show the results of propagation simulations [56] for the case of a backfilled chamber and for an interaction length of 2 mm. (c) The measured peak phase shift for $\mathbf{E}_{pump} \parallel \mathbf{E}_{probe}$ as a function of peak intensity for Ar (×) and N$_2$ (O). The calculated peak phase shift in Ar using the higher-order Kerr coefficients given in Ref. [10] is shown as a dashed line.

The bound electron optical nonlinearity in Ar is instantaneous to a very good approximation because the energy of the lowest electronic excitation is 15 eV, far greater than the photon energy 1.5 eV. The ordinary instantaneous Kerr effect is linear in the intensity I: The refractive index is of the form $n = n_0 + n_2 I$, where n_0 is the index of refraction and n_2 is the Kerr coefficient, and thus $\Delta\phi(x,t) \propto I_{pump}(x,t)$. The measured FWHM in Fig. 4.1(a) of 38 fs matches an autocorrelation measurement of the pump pulse. The spatial profile lineout, shown in Fig. 4.2(b), agrees well with the pump spot profile. This confirms that the intensity profile in the thin gas target is the same as the vacuum profile. The deleterious effect of excessive interaction length on the width of the response is illustrated in Fig. 4.1(b). A lineout of the measured phase shift along x at $t = t_{pump}$ is shown with the chamber backfilled with Ar—note the wider profile compared to the flow tube case. Also shown are simulations of $\Delta\phi\left(x, t_{pump}\right)$ using the beam propagation method [56]; with the simulation we obtain an effective pump-gas interaction length of 2 mm, in agreement with the tube geometry. Because of the short interaction length, intensity clamping [2] does not affect the intensity profiles.

The peak phase shift measured in the experiment is plotted as a function of peak intensity in Fig. 4.1(c). We find a linear dependence for both Ar and N_2 and nearly the same Kerr coefficient, which is consistent with other experiments [70]. For peak intensity I_{peak} = 60 TW/cm^2, we measure a peak phase shift in Ar of 0.059 rad. For a medium with an effective interaction length L_{eff} , $\Delta\phi_{peak} = 2 \times 2\pi L_{\mathrm{eff}} n_2 I_{peak}/\lambda$ (note the extra factor of 2 because we measure cross phase modulation [51]). Using the value from our absolute measurement for Ar, n_2 = 9.7×10^{-20} cm^2/W [70, 71] at 1 atm, and using $L_{\mathrm{eff}} \approx 2$ mm, we estimate an average pressure in the interaction region of 0.3 atm.

A higher-order Kerr effect would add terms of the form $n_{2m}I^m(t)$, where m > 1 [10]. No negative instantaneous phase is observed at any intensity in Ar or N_2, nor do we see evidence of saturation [10], in disagreement with the results of Loriot *et al.* [10]. A simulation of the phase shift expected by using the coefficients reported in Ref. [10] is shown as a dashed line in Fig. 4.1(c). The difference is stark and well outside any error in our experiment we can conceive of. We have also performed the same experiment in Ar by using a probe pulse whose spectrum overlaps the pump pulse, with orthogonal polarization so that the pump light could be rejected by a polarizer before the spectrometer [72]. A monotonically increasing instantaneous phase shift is observed up to the ionization threshold.

We have studied the possible origin of the results obtained in Ref. [10] and have found that the interference of pump and probe pulses of the same wavelength can produce a plasma grating which gives rise to an effective birefringence [50].

Increasing the pump intensity beyond the level of Fig. 4.1 requires careful consideration of increased supercontinuum generation by the pump itself. Because the pump and probe paths are not phase stable with respect to one another, spectral fringes between the pump supercontinuum and the reference pulse average out when many interferograms are summed. So the pump supercontinuum does not cause significant data distortion until it saturates the CCD camera, which occurs at intensities higher than 200 TW/cm^2, well beyond the ionization threshold of ~100 TW/cm^2 [73, 74]. Maps showing $\Delta\phi(x,t)$ at high intensity in Ar are shown in Fig. 4.2. At high intensities we observe an additional response due to the plasma generated by ionization [75]. The plasma produces a negative index contribution $\Delta n_{plasma} = -N_e/2N_{cr}$, where N_e is the electron density and N_{cr} is the critical density. The plasma densities measured are consistent with calculations using Ammosov-Delone-Krainov rates [76]. Plots of $\Delta\phi\left(x_{pump},t\right)$ as a function of pump intensity are shown in Figs. 4.2(c) ($\mathbf{E}_{\mathrm{pump}} \parallel \mathbf{E}_{\mathrm{probe}}$) and 4.2(d) ($\mathbf{E}_{\mathrm{pump}} \perp \mathbf{E}_{\mathrm{probe}}$).

Note that the plasma contribution seen in Fig. 4.2 is highly characteristic: (i) Its onset at higher intensity (180 TW/cm^2 compared to 120 TW/cm^2) increasingly dominates the instantaneous Kerr response at the back of the pulse; the residual positive Kerr peak appears to move forward in time; (ii) unlike the Kerr response, the plasma induced phase shift is probe polarization independent; and (iii) after generation, the plasma response is long-lived on the time scale of this measurement, owing to recombination times of the order of ~100 ps.

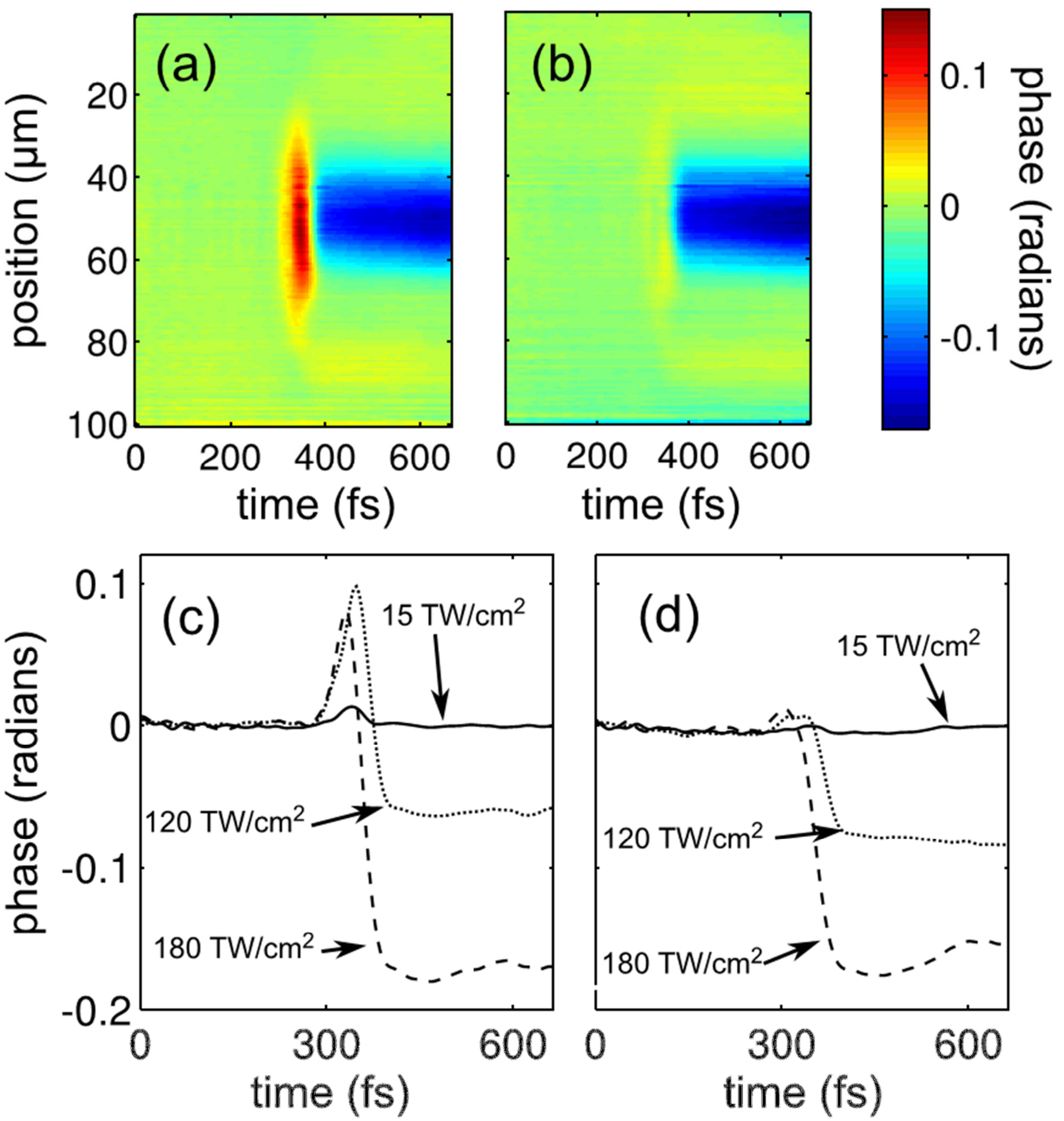

Figure 4.2 Experimental data for Ar. (a),(c) $\mathbf{E}_{pump} \parallel \mathbf{E}_{probe}$. (b),(d) $\mathbf{E}_{pump} \perp \mathbf{E}_{probe}$. (a),(b) Extracted phase $\Delta\phi(x,t)$ at 150 TW/cm^2 vacuum pump intensity, showing the positive electronic Kerr effect signal at $t = t_{\mathrm{pump}}$ and the negative plasma signal at later time delays. (c),(d) Lineouts $\Delta\phi(x_{\mathrm{pump}}, t)$ as a function of pump intensity. Within error, the plasma response is constant in time after the pump has passed; we observe increased noise at the edges of the time window due to the decreased magnitude of the probe and reference spectra on the wings. The curves at 120 and 180 TW/cm^2 give approximate electron densities N_e=7×10^{15} cm^{-3} and N_e=2×10^{16} cm^{-3}, respectively.

In N_2, the optical Kerr response has an additional contribution from the transient alignment of the molecules in the strong optical field [7, 20, 21]. Results for N_2 are shown in Fig. 4.3; $\Delta\phi(x,t)$ is shown at low pump intensity for parallel and perpendicular polarization in Figs. 4.3(a) and 4.3(b), respectively.

The index change is $\Delta n(t) = n_2 I(t) + \int_0^{\infty} R(t') I(t-t') dt'$, where $R(t)$ is a response function that depends on properties of the rotational levels and the nuclear spin statistics [7, 21]. In N_2 the rotational response peaks about 80 fs after the pump pulse arrives, as can be seen in Fig. 4.3(a). The ratio of the instantaneous Kerr effect for parallel to perpendicular polarization is 3:1 in an isotropic medium. For the rotational component, the ratio is 2:-1. The different symmetry properties allow the clean separation of the two contributions, as shown in Fig. 4.3(c).

Previous measurements using this technique [20, 21] were unable to resolve the two contributions, but here we can owing to the shorter pump pulse. To our knowledge, this is the first direct observation of the relative contributions of the instantaneous and rotational components of the Kerr effect in N_2. At higher intensities plasma is observed, as shown in plots of $\Delta\phi(x_{pump}, t)$ in Figs. 4.3(d) and 4.3(e).

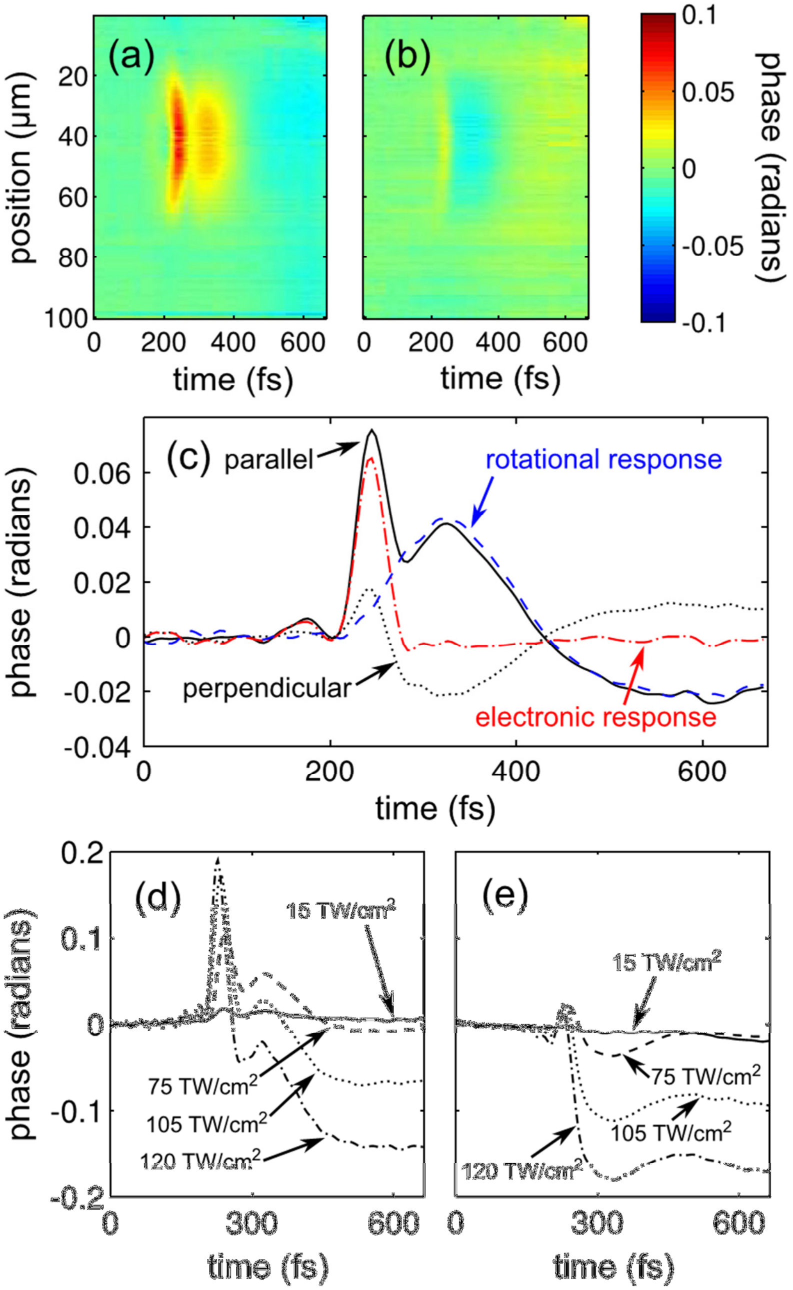

Figure 4.3 Experimental data for N_2. (a),(d) $\mathbf{E}_{pump} \parallel \mathbf{E}_{probe}$. (b),(e) $\mathbf{E}_{pump} \perp \mathbf{E}_{probe}$. (a),(b) Extracted phase $\Delta\phi(x,t)$ at 60 TW/cm^2 pump intensity, showing the positive instantaneous Kerr effect (coincident with the pump) and the rotational response at later time delays. (c) Lineouts $\Delta\phi(x_{\text{pump}},t)$ for the data shown in (a),(b). The decomposition of the signal into instantaneous and rotational components, as described in the text, is also shown. (d),(e) Lineouts $\Delta\phi(x_{\text{pump}},t)$ as a function of pump intensity.

4.2 Direct measurement of gas nonlinearity in noble gases

In this section, we present a series of SSSI results for the noble gases He, Ne, Ar, Kr, and Xe. We average 1000 interferograms before performing the extraction, allowing measurement of phase shifts as small as 5×10^{-3} rad.

Figure 4.4 (left panel) shows two $\Delta\Phi(x,t)$ traces for Ne, one at a peak intensity below where plasma is generated and one just above.

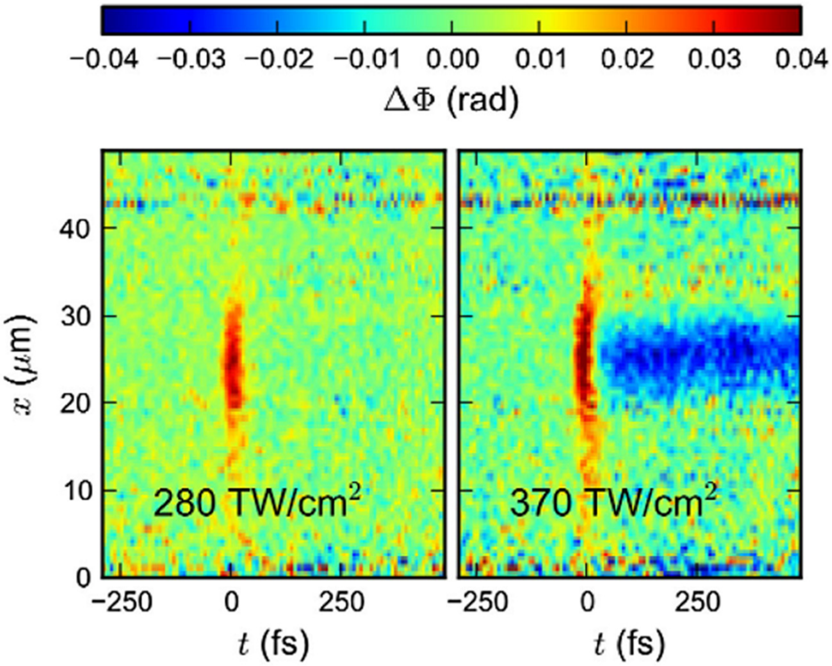

Figure 4.4 Probe phase shift $\Delta\Phi(x,t)$ measured in neon using SSSI, for an intensity below (left) and above (right) the onset of ionization.

Here, the L_{eff} is 200–400 μm, depending on the gas used. Again, folded wavefront interferometry allowed extraction of the absolute linear phase shift of the Ar stationary gas flow; all other gases were referenced to Ar, providing absolute calibration of $\Delta\Phi(x,t)$. The absolute index shift is calibrated by a measurement in a backfilled vacuum chamber at low pressure, as described in chapter 3.

The result of our experimental values of Δn measured up to the ionization threshold in each gas is shown in Fig. 4.5 (note that the ionization threshold in Ar measured here is lower by about 20% than that found in sec. 4.1, due to an overestimation of the peak intensity in that experiment).

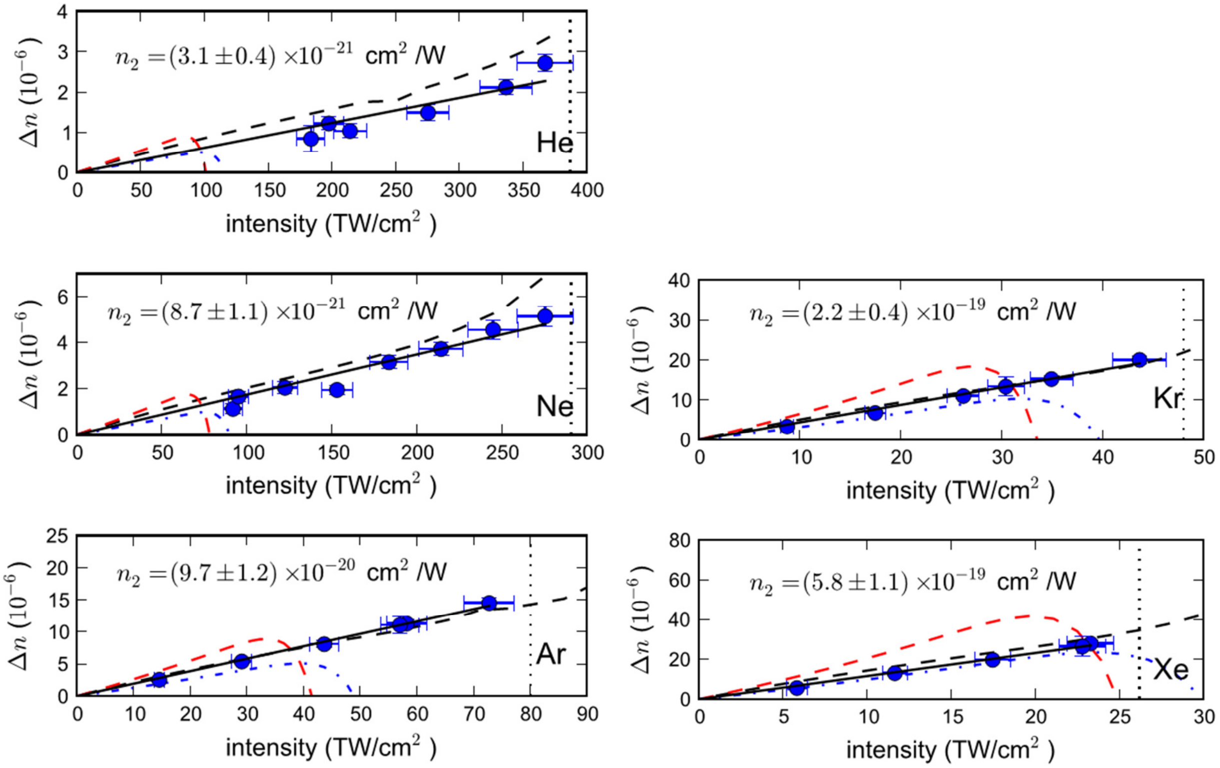

Figure 4.5 The nonlinear refractive index Δn of the noble gases experienced by a weak probe pulse as a function of pump laser peak intensity. Blue dots show experimental data points, and the solid line shows a linear fit of the data to $2\,n_2 I$. Vertical dotted lines show, for each gas, the measured ionization threshold. The dashed black line is a Kramers-Kronig (KK) calculation, detailed in [49]. The red dashed line is the result from Brée *et al.* [46]. The blue dash-dotted line is the self-refractive index plotted in Brée *et al.* Horizontal error bars denote uncertainty in the intensity calibration and vertical error bars denote uncertainty in the phase extraction.

The experimental results clearly confirm $\Delta n \propto I$ up to the ionization threshold, a remarkable result given that perturbation theory is hardly applicable at these intensity levels. The experimentally measured values of $n_2 = \Delta n/2I$ are in good agreement (the factor of 2 recognizes that Δn describes cross-phase modulation) with previous estimates using harmonic generation ([12] and references therein), and are also close to the Kramers-Kronig (KK) prediction in all cases [49]. Note that no adjustable parameters were used in the experimental analysis or in the KK calculation [49].

4.3 Degenerate, chirped pulse spectral interferometry

To resolve the HOKE controversy, Wahlstrand *et al.* proposed the plasma grating theory based on two-beam coupling to explain the features observed in Loriot's experiment [50, 51]. Several experiments were performed to verify the theory [51, 52].

The key conclusion of this plasma grating theory is that when the pump intensity is near the ionization threshold, the pump beam can be diffracted into the probe direction by a nonlinear refractive index grating produced by interference between the two beams. This diffraction results in a negative *phase shift* to the probe polarization component that is *parallel* to the pump field direction and, therefore, effective negative birefringence. The grating phase shift only appears when the pump and probe beams are *degenerate* (the spectra of pump and probe pulses overlap with each other).

Based on a numerical calculation in atomic hydrogen, Béjot *et al.* recently argued that the higher-order Kerr effect is present only at optical frequencies near the frequency of an intense driving field [77], and therefore nondegenerate pump-probe experiments, which use a probe pulse detuned from the pump pulse frequency, are incapable of observing it.

In this section we describe new experimental evidence that the negative, nearly instantaneous signal observed using a degenerate probe is caused by the plasma grating.

To further investigate the origin of the negative birefringence, we use spectral interferometry with a nearly degenerate probe pulse. The principle of the degenerate experiment is identical to our previous nondegenerate implementation using a supercontinuum probe [20]. The challenge in performing the experiment with a degenerate probe is rejecting pump light from the detection spectrometer. We previously reported data using a degenerate probe with a polarization perpendicular to the pump, where polarizers were used to block the pump light before detection [72]; in this study, the result is identical to that found with a collinear geometry.

Here, we use a noncollinear geometry and reject pump light using an aperture, allowing orientation of the pump polarization parallel to the probe. A sketch of the experimental apparatus is shown in Fig. 4.6(a). The pump is a 40 fs FWHM pulse centered at 800 nm. The pump and probe (or reference) beams cross at 3°, allowing the pump beam to be blocked before probe detection. The two beams are crossed inside a vacuum chamber backfilled with 0.5 atm of Ar. The probe and reference pulses are chirped using a block of glass to a group delay dispersion of 1650 fs^2.

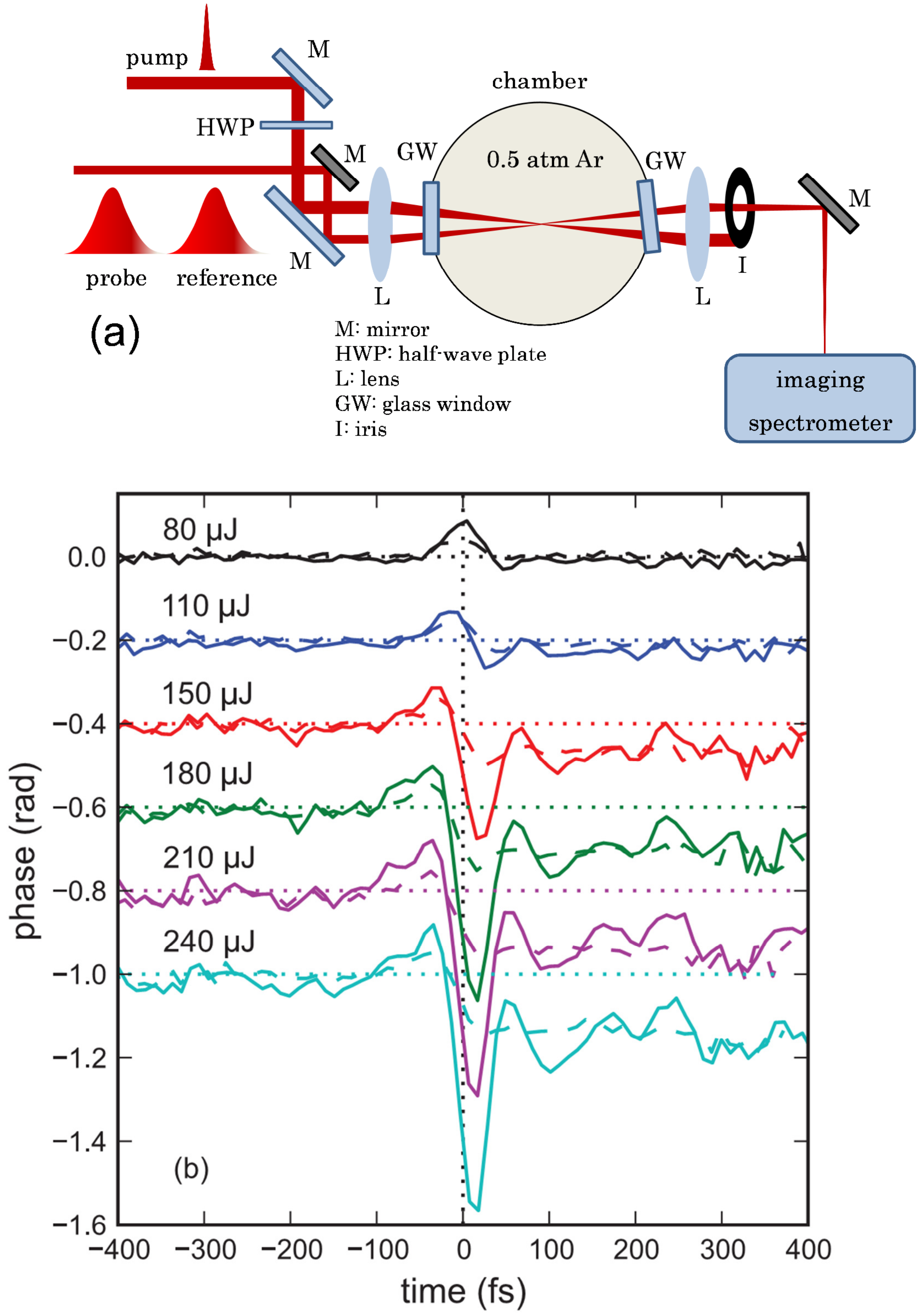

Figure 4.6 Degenerate spectral interferometry results. (a) Experimental setup. (b) Extracted time domain phase shift as a function of the pump pulse energy for parallel polarizations (solid) and perpendicular (dashed).

Results of the experiment are shown in Fig. 4.6(b). We observe a positive instantaneous phase shift near the time of peak pump intensity ($t = 0$) due to the optical Kerr effect, and a negative, long-lasting signal from electrons freed by ionization. When the pump beam is polarized parallel to the probe beam, we in addition observe a negative signal near $t = 0$ that is much larger than the positive Kerr signal at high intensity. We attribute the oscillations in the data to interference between supercontinuum generated by the pump pulse and the probe pulse. It is important to note that as the intensity is increased, the negative signal at $t = 0$ appears simultaneously with the smooth plasma signal. This is strong evidence for the plasma grating interpretation.

4.4 Conclusion

In summary, we have performed direct measurements of the optical Kerr effect in the inert gases (He, Ne, Ar, Kr and Xe) and N_2 using single-shot supercontinuum spectral interferometry. In N_2, we are able to distinguish between instantaneous and rotational components of the nonlinearity, and the polarization dependence is consistent with theory. We observe the usual optical Kerr effect, linear in the intensity, as well as the onset of plasma, but no higher-order instantaneous nonlinearities effecting either saturation or negative response. The fact that the pump-induced response appears to be linear in the intensity until the point of ionization is a reflection of the latter’s extremely nonlinear onset. At least for 38 fs pulses, there is no practical distinction between plasma and special atomic states contributing to negative polarizability. These results disprove the idea that higher-order instantaneous nonlinearities are important in nonlinear optics in gases at high intensity.

In addition, we have presented results of the noncollinear degenerate pump-probe spectral interferometry experiments for the specific purpose of investigating the effect on a probe pulse of the nonlinear interference grating. The results reinforce the idea that, for the purpose of measuring the nonlinear response of a medium using cross-phase modulation, a nondegenerate pump-probe experiment is preferable to a degenerate one.

Consequently, our results strongly confirm the long-standing conceptual picture [2] that short pulse filamentation in gases arises from the interplay between nonlinear self-focusing from bound electron nonlinearities and defocusing due to plasma generation.

Chapter 5

Gas hydrodynamics driven by nonlinear absorption of femtosecond laser pulses

The experiment we present in this chapter consists of three parts. In the first part, we demonstrate the effect of laser pulse repetition rate on the self-focusing collapse and filament spectrum as a function of propagation distance in room air. In the second part, we examine the effect of pulse repetition rate on supercontinuum generation in a Xenon gas cell. In the third part, we present results of longitudinal interferometry measurements of long timescale gas evolution after femtosecond laser interaction. We then present simulations of the density hole evolution and use those results to gain physical insight and interpret our experiments.

5.1 Effects on experiments depending on gas nonlinearity: supercontinuum generation and filamentation

For all experiments, the laser pulses were generated by a 1 kHz Ti:sapphire laser system capable of producing up to 3.5 mJ, 40 fs near infrared pulses centered at 800 nm. For the air filament experiment we used 0.9-1.5 mJ laser pulses focused at f/600 with a 3 m lens. The filament core spectrum was measured as a function of propagation distance by scanning a rail-mounted pinhole along the propagation path and collecting the forward emission on the exit side. The pinhole was prepared prior to the experiment by drilling a ~300 μm diameter hole in a thin Teflon sheet with the 1 kHz filamenting beam at multiple axial locations. This guaranteed negligible further pinhole erosion during a full axial scan. The filament was generated on an enclosed optical table to minimize shot-to-shot transverse position movement from air currents in the laboratory. The filament propagation terminates within ~2 mm past the pinhole exit. Simulations using the propagation code of ref. [26] show that no additional nonlinear frequency broadening is imparted beyond this point. Therefore, the collected spectrum is that of the propagating laser at the filament core. For this experiment, the laser was operated at 1 kHz but the repetition rate for focused pulses was controlled with chopper wheels synchronized to the laser timing. We found earlier that controlling the repetition rate with the laser's regenerative amplifier Pockels cell resulted in slight thermally-induced changes to the beam intensity profile and phase front which were sufficient to affect the filamentation collapse location.

The filament core spectrum as a function of axial position for three laser repetition rates and pulse energies is shown in Fig. 5.1.

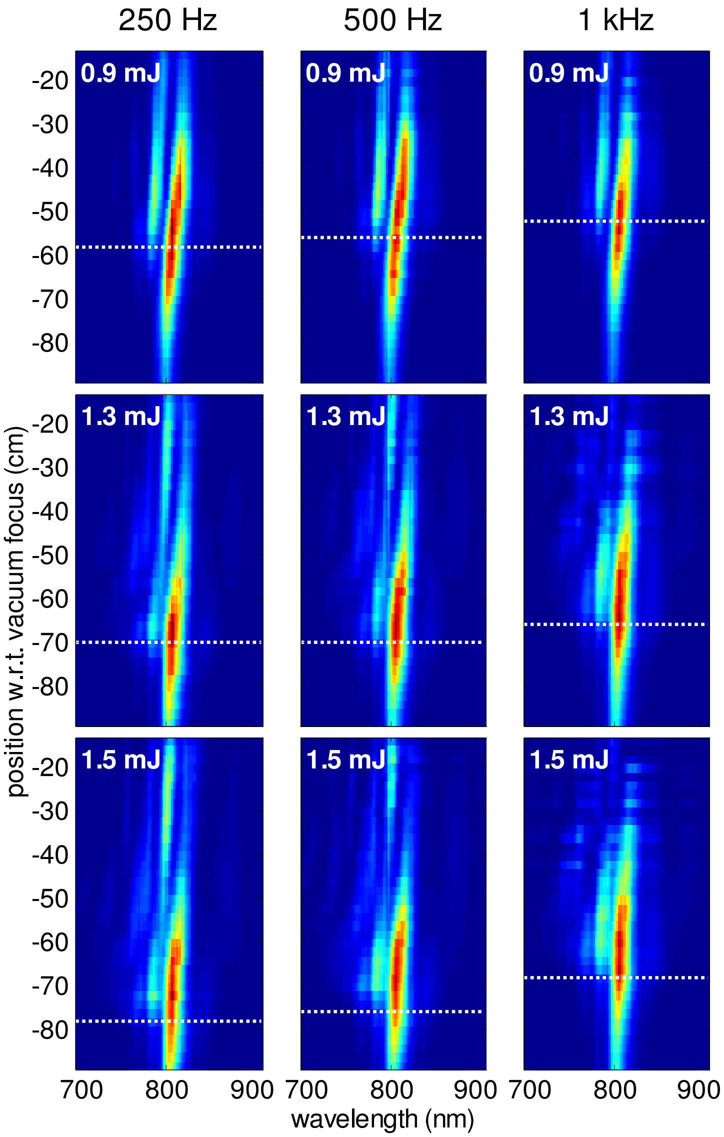

Figure 5.1 Filament core spectrum vs. propagation distance as a function of pump energy and repetition rate. Propagation distance is measured with respect to the vacuum focus. The laser pulse propagates from below in these panels. The white dotted line shows the position of beam collapse to a filament.

The laser pulse propagates from below. In each panel, the axial location of beam collapse to a filament, which is identified as the beginning position of the additional blue-side spectrum wing, is shown with a dotted line. This was observed by recording the axial location where plasma fluorescence begins and is coincident with the onset of a strong blue shift owing to gas ionization. It is seen that the collapse position moves farther from the lens as the pulse repetition rate increases from 250 Hz to 1 kHz, and this axial shift increases with pulse energy. The onset of spectral blue wings, the signature of plasma generation, follows this axial shift, and the extent of the blue wings increases with repetition rate, especially for the higher energy pulses.

We next investigated a very common arrangement in many labs that use high repetition rate lasers (typically 1 kHz) to generate supercontinuum spectra for compression or other applications [27-32]. Here, we focused 140-250 μJ pulses at f/100 into a gas cell filled with 2.2 atm Xenon, and examined the repetition rate-dependence of supercontinuum generation. The cell windows were sufficiently far from the beam waist that they contributed negligibly to the generated spectrum. The results are shown in Fig. 5.2.

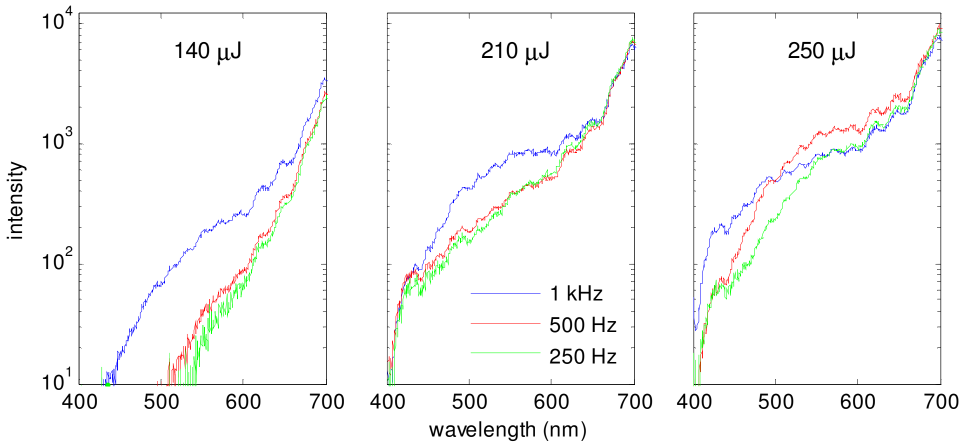

Figure 5.2 Supercontinuum spectra vs. laser pulse energy and repetition rate.

A normal incidence 800 nm dielectric mirror was used to filter the pump from the spectrum. It is seen that in all cases, the bluer parts of the spectra are dominant for the highest repetition rates, with the effect strongest at 140 μJ pump energy. The blue wing augmentation is even stronger than in the air filament case of Fig. 5.1.

5.2 Measurements and simulations of gas density hole evolution

To understand the origin of these repetition rate dependent effects, we performed longitudinal interferometry on femtosecond filament-excited gas. For this experiment, we operated the pump laser at 20 Hz (50 ms between pulses) in order to measure the long timescale gas dynamics driven by a single pump pulse. Since the results from the filament and supercontinuum experiments (Figs. 5.1 and 5.2) indicate possible dependence on a gas evolution timescale ranging up to milliseconds, we could not use a standard optical pump-probe delay line. Instead, we used a gated CCD camera and a continuous probe beam from a 635 nm CW diode laser which counter-propagated through the pump-excited interaction region, overlapping the pump beam. The setup is shown in Fig. 5.3.

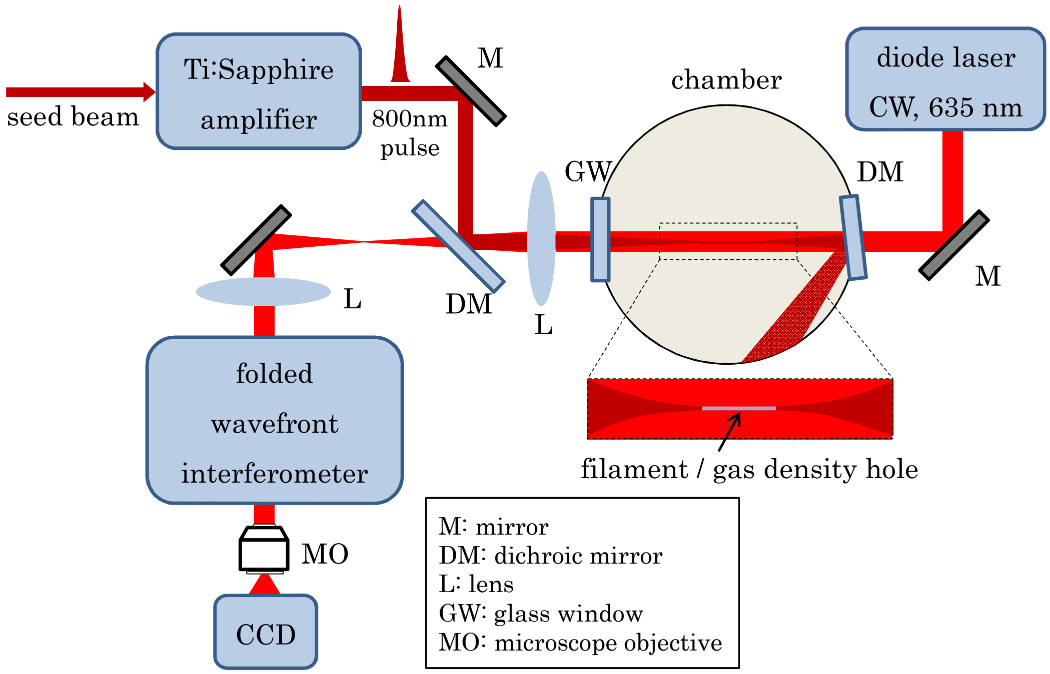

Figure 5.3 Interferometry setup. The CW diode probe laser counter-propagates with respect to the pump beam direction, passes through the pump focusing lens, and enters the folded wavefront interferometer.

The probe passed back through the pump focusing lens, was separated from the pump beam with a 800 nm dielectric mirror (DM), and then was sent through a folded wavefront interferometer [57, 58]. The vacuum focal plane of the pump laser beam was imaged onto a CCD camera at the exit of the interferometer. Temporal gating of the probe was obtained by triggering the CCD camera's electronic shutter with an adjustable delay with respect to the pump pulse. We used the minimum temporal window of the electronic shutter of ~40 μs, which set the time resolution. As will be seen, this resolution is sufficient for measuring the long timescale gas response to the femtosecond pump pulse.

The linearly polarized 40 fs pump pulse was focused at f/65 into the chamber backfilled with various pressures of Kr, O_2, N_2, Ar, and air. The laser spot full width at half maximum (FWHM) diameter was ~60 μm. The pulse energy was adjusted using a set of half-wave plate (HWP) and thin-film polarizer (TFP). Figure 5.4(a) shows, for pump energy 0.72 mJ, a sequence of gas density profiles in 1 atm air extracted from the interferograms using well-known fringe analysis techniques [58]. The inset in the upper left of the figure shows the time-dependent phase shift imposed on a collinear spectral interferometry probe in a temporal window centered on the pump (our spectral interferometry diagnostic is described in references [21, 48]). For later hydrocode simulations, the initial electron density of $\sim 1.4\times 10^{16}$ cm^{-3} is extracted from the phase shift ~0.6 ps after the pump pulse.

By the first frame shown in the sequence, at 40 μs delay after the pump, the plasma has long ceased to exist, as it will have recombined well before ~10 ns [72, 78]. The 2D gas density profile is an average over the CW probe laser's interaction length. The density profile is extracted from the 2D phase shift profile, the known linear polarizabilities of nitrogen and oxygen [79] and an interaction length L of ~18 mm, determined by the axial extent of the filament's plasma fluorescence:

$$\Delta\phi \cong \frac{2\pi}{\lambda}\left(\frac{\Delta N\,\alpha}{2}\right)L. \tag{5.1}$$

Simulations of the probe beam propagation using the beam propagation method [80] show negligible refractive phase front distortion that could complicate interpretation of our 2D phase extraction.

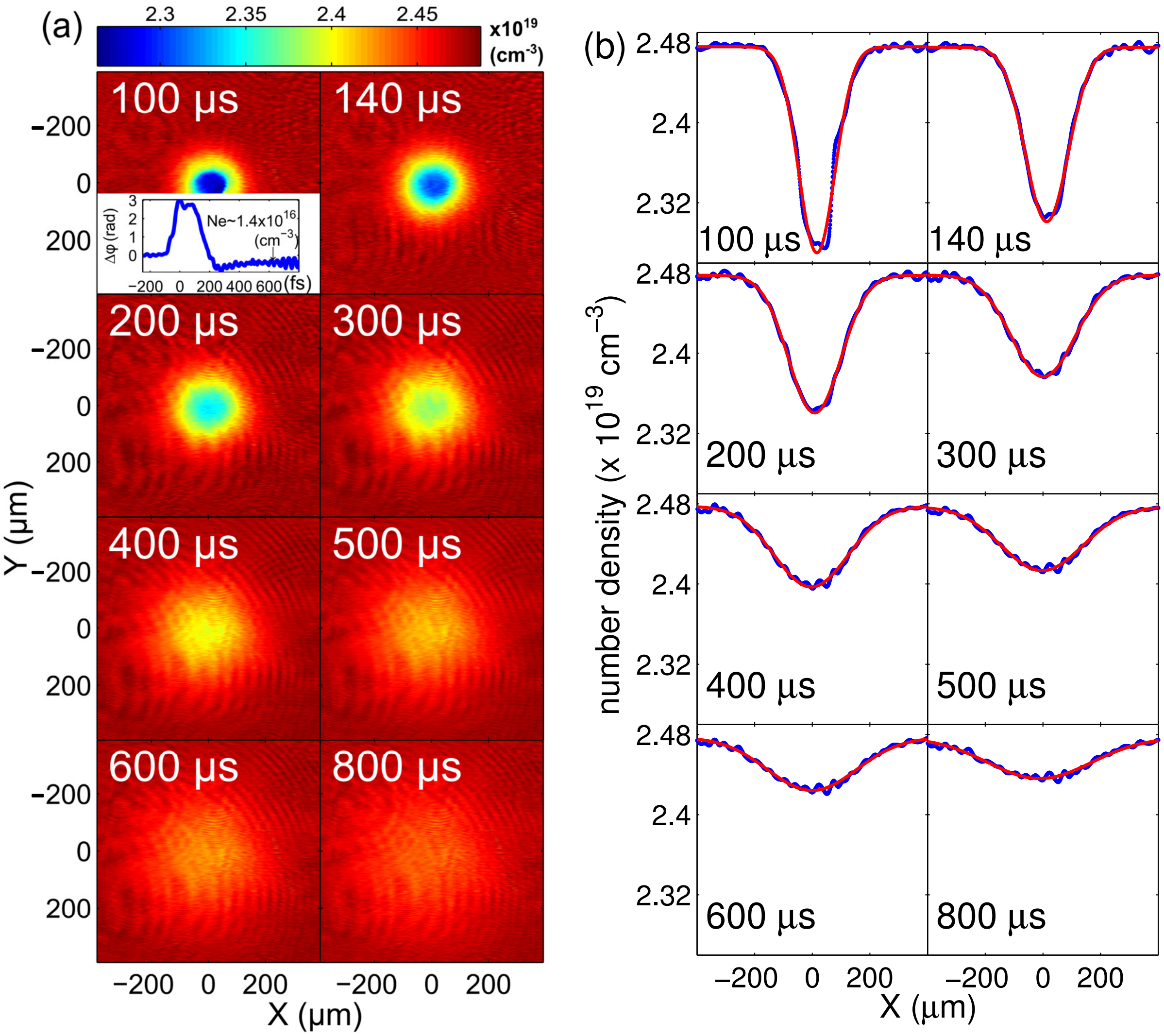

Figure 5.4 (a) Gas average number density profiles vs. probe delay with respect to interaction of a 800 nm, 0.72 mJ, 40 fs pulse focused at f/65 into air at 1 atm. The inset shows electron density measured with spectral interferometry [21, 48]. (b) Lineouts of the air density profiles of Fig. 5.4(a). The blue curve is the measurement; the red curve is a Gaussian fit. The spatial resolution of the interferometric images is 10 μm. Density was extracted from phase shift maps using the linear polarizabilities of N_2 and O_2 , β_{N2}= 1.76 ×10^{-24} cm^3 and β_{O2}= 1.60 ×10^{-24} cm^3 [79].

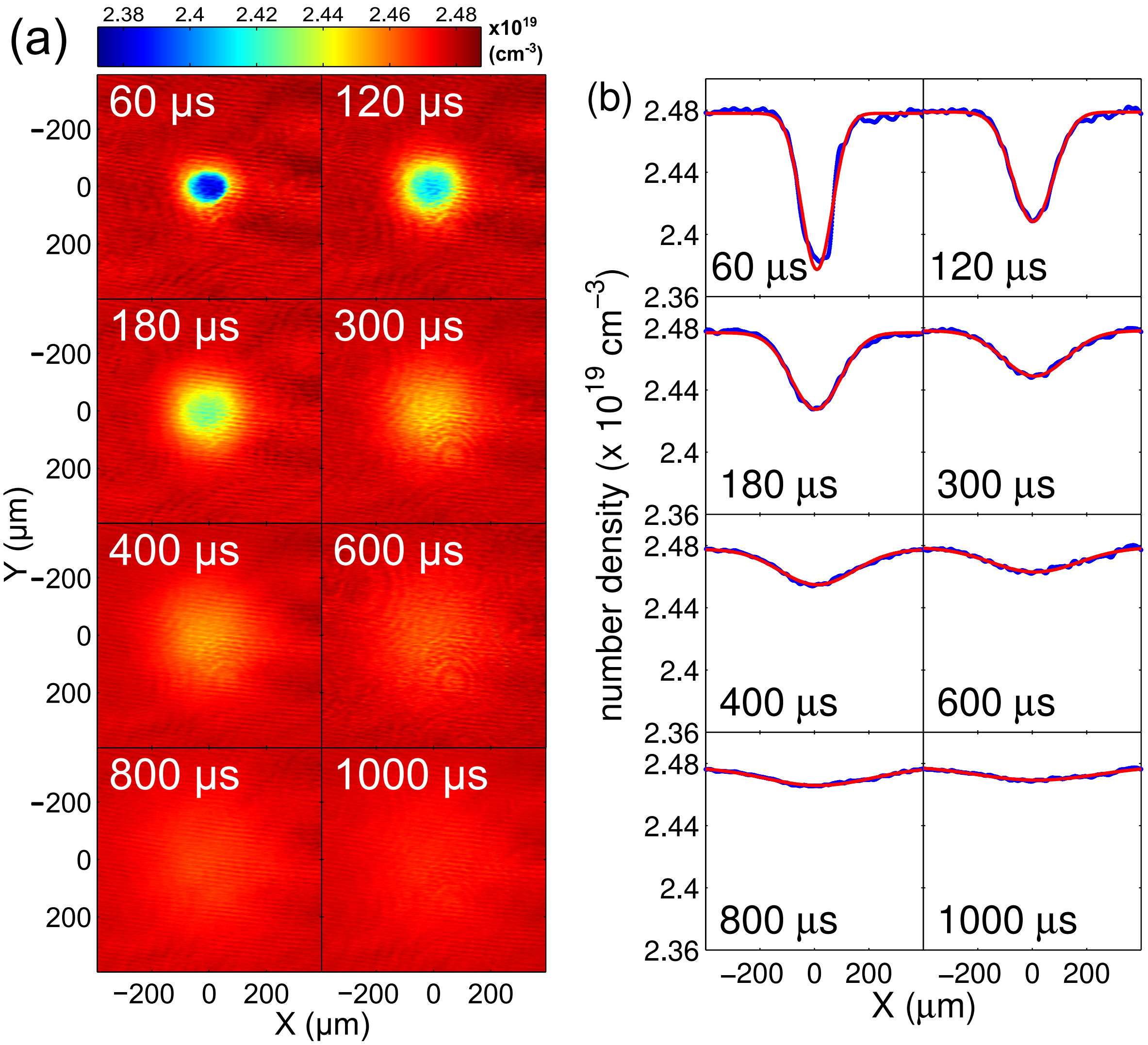

Figure 5.5 (a) Number density profiles vs. probe delay with respect to interaction of a 800 nm, 0.72 mJ, 40 fs pulse focused at f/65 into N_2 at 1 atm. (b) Lineouts of the N_2 density profiles of Fig. 5.5(a). The blue curve is the measurement; the red curve is a Gaussian fit. The spatial resolution of the interferometric images is 10 μm. Density was extracted from phase shift maps using the linear polarizabilities of N_2 and O_2 , $\beta_{N2}= 1.76 \times 10^{-24}$ cm^3 [79].

Corresponding lineouts of the gas density are shown in Fig. 5.4(b), with Gaussian fit curves overlaying the data curves. The profile sequence shows the gas density hole widening and becoming shallower. By ~0.5 ms, there is only a ~1% density depression remaining. Figures 5.5(a) and (b) show similar plots for 1 atm of N_2. Qualitatively similar results occur for the other gases and pressures used.

To gain an understanding of the density hole evolution on gas type, pressure, and pump laser parameters, we performed simulations of the gas hydrodynamic evolution in cylindrical geometry using a one-dimensional Lagrangian one-fluid hydrocode, in which the conservation equations for mass, momentum and energy, $\partial\xi_i/\partial t + \nabla\cdot(\xi_i\mathbf{v} + \phi_i) = S_i$, were solved numerically. The mass equation has $\xi_1 = \rho$ and $\phi_1 = 0$, the momentum equation has $\xi_2 = \rho\mathbf{v}$ and $\phi_2 = P\overleftrightarrow{\mathbf{I}}$ (where $\overleftrightarrow{\mathbf{I}}$ is the unit tensor), and the energy equation has $\xi_3 = \varepsilon + \frac{1}{2}\rho\mathbf{v}^2$ and $\phi_3 = P\mathbf{v} + \mathbf{q}$. Here, ξ is the volume density of the conserved quantity, ϕ is the flux of that quantity, and S refers to sources or sinks, while ρ is mass density, ε is fluid internal energy density, $\mathbf{v}$ is fluid velocity, P is gas pressure, and $\mathbf{q}$ is the heat flux. At all times, $S_1 = S_2 = 0$ owing to mass and momentum conservation, but $S_3 \neq 0$ because the thermal part of the energy density is changed by laser heating and by ionization/recombination of all the relevant species in the gas.

Solving the full set of fluid plus species population equations from the femtosecond through millisecond timescales requires accurate microscopic rates, including those for inelastic collisions, ionization, attachment, and recombination from the initial plasma at ~5 eV down to room temperature. Many of these rates are not well known. Furthermore, in principle one must keep track of all the species involved (atoms, ions, molecules, molecular ions) and their various states of excitation.

We can, however, proceed by recognizing that at times >>10 ns after laser excitation, all of the energy initially stored in free electron thermal energy and in the ionization and excitation distribution has been repartitioned into an essentially fully recombined gas in its ground electronic state. If the gas is molecular, for the conditions of our experiments it will also be in the ground vibrational state and in a thermal distribution of rotational states. Because the thermal conductivity of neutral gas is much smaller than that of plasma, the total energy initially deposited by the femtosecond laser pulse remains contained within a diameter comparable to the original laser spot size.

Before electron-ion recombination, the free electrons diffuse radially outward. However, part of the electron energy is passed to ions: the Coulomb electric force between them decelerates electrons and accelerates ions, finally they flow with about the same speed and maintain the quasi-neutrality condition; this process is called ambipolar diffusion [81]. This sudden hydrodynamic expansion is accompanied by the generation of a radial sound wave.

As the ambipolar diffusion during the recombination process is much less than the laser spot width of ~50 μm, the 'initial' radial pressure distribution driving the gas hydrodynamics at times >10 ns is set by the initial plasma conditions $P_0(r) = N(r)k_BT(r) \approx \left(\frac{f_e}{f_g}\right)N_e(r)k_BT_e(r)$, where k_B is Boltzmann's constant, $N_e(r)$ and $T_e(r)$ are the initial electron density and electron temperature profiles immediately after femtosecond laser pumping of the gas, and $N(r)$ and $T(r)$ are the neutral gas number density and temperature profiles. This expression depends on the thermodynamic degrees of freedom of the free electrons (f_e = 3 translational degrees of freedom) and the gas, f_g, which depends on the gas type and temperature.

In addition, an initial radial velocity profile with a weak positive gradient is imposed to mimic the results of our full hydrodynamic simulations at times <10 ns. In practice, our long timescale simulation results are insensitive to the detailed shapes of either the initial pressure profile or the fluid velocity profile, and depend mostly on the peak initial electron density and temperature and the radial scale length.

To simulate the neutral gas response at long timescales we solve the fluid equations for the ξ_i, using $S_3 = 0$ and the initial pressure profile given by $P_0(r)$ above. We expect the fluid velocity field to relax over a timescale $\tau_{relax} \sim R_0/c_s$, where R_0 is the initial radial scale of the laser heating, given by the laser spot radius, and $c_s = (k_B T/m)^{1/2}$ is the gas sound speed, where m is the atom or molecule mass. For R_0~50 μm, N_e~1.5×10^{16} cm^{-3} and $k_B T_e$ ~ 5 eV (typical filament electron density and temperature (see below)), and N ~ 2.5×10^{19} cm^{-3} for a 1 atm ambient gas, we find ΔT~100 K as a result of repartitioning and τ_{relax} ~1 μs. As we shall see, this timescale is borne out by the fluid simulations: for all gases and pressures of this experiment, by a few microseconds after the laser interaction, the fluid velocity field has relaxed and the pressure becomes constant with radial position. A quasiequilibrium is reached where the gas density profile is then just the inverse of the temperature profile, and further evolution is described by thermal diffusion.

To understand the earlier time evolution of the gas before the thermal diffusion-dominated phase, Fig. 5.6 shows simulation results in 1 atm N_2 capturing the dynamics at times <10 μs after the pump pulse. We used N_e=1.5×10^{16} cm^{-3} and $k_B T_e = 5$ eV as the initial plasma conditions as the source of thermal energy repartitioned into the atmospheric pressure neutral gas. While there are direct measurements of filament electron density (see Fig. 5.4(a) and ref. [17]), we rely on measurements of <10 eV electron spectra [82] from above threshold ionization in dilute nitrogen gas for laser intensity <10^{14} W/cm^2. As will be seen, the good agreement between measurements and simulations of the gas density hole justify this choice of initial electron temperature. The repartitioning of the plasma energy to neutral gas assumes 3 degrees of translational freedom of the molecules $\left(3 \times \frac{1}{2} k_B T\right)$ plus 2 degrees of rotational freedom $\left(2 \times \frac{1}{2} k_B T\right)$, so that $f_g = 5$. The resulting gas temperature change (ΔT~100 K) is insufficient for excitation of significant molecular vibration. It is seen that by ~1 μs, a sound wave has separated away from the interaction region and propagates to the simulation (absorbing) boundary, and by ~2 μs, a quasi-stationary density hole is established, in agreement with our earlier estimate for this timescale.

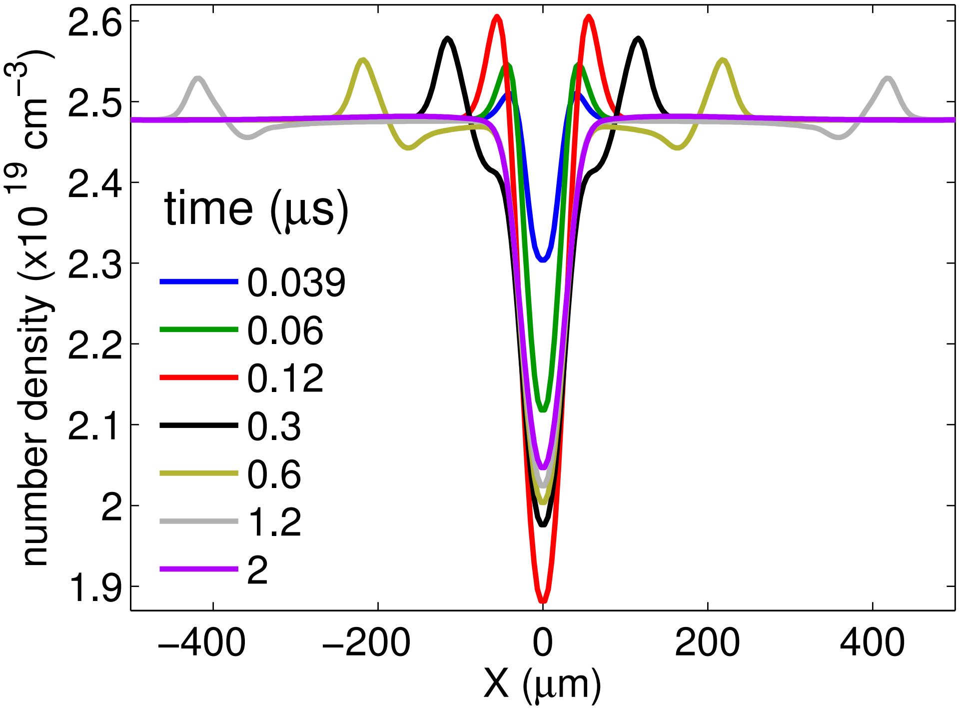

Figure 5.6 Hydrodynamic simulation of the early phase of gas evolution of 1 atm N_2. Initial conditions are N_e=1.5×10^{16} cm^{-3} and $k_B T_e$ = 5 eV. The density profile becomes quasi-stationary by ~2 μs.

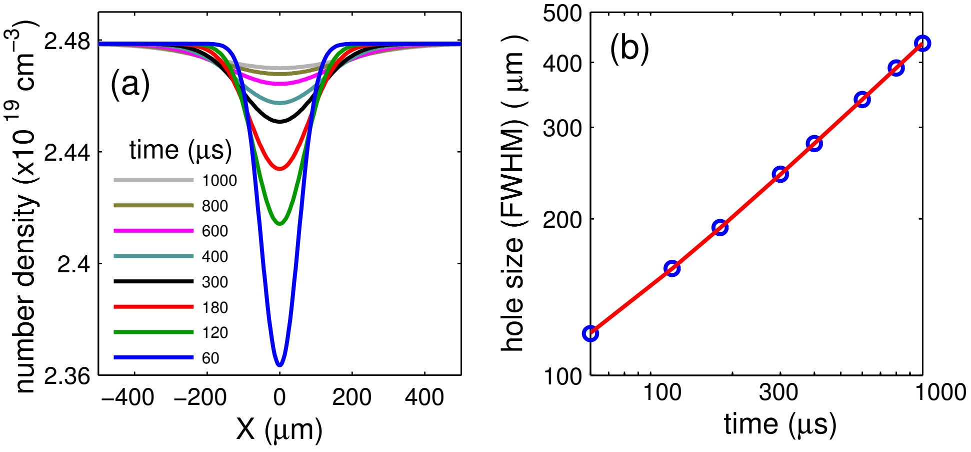

Figure 5.7 (a) Simulated evolution of the gas density hole at later times. (b) Hole FWHM $d_{1/2}$ vs. time. The red curve is a fit to $d_{1/2} = (R_0^2+4\alpha t)^{1/2}$ indicating that the long time evolution of the gas is thermal diffusion dominated.

Figure 5.7(a) shows simulation results for times up to 1 ms for the same conditions as in Fig. 5.6. Good agreement is seen with the experimental N_2 density profiles of Fig. 5.5. In Fig. 5.7(b), we plot the hole FWHM diameter $d_{1/2}$ as a function of time. At these long times, the gas density profile evolution is governed completely by thermal diffusion, as indicated by the time dependence $d_{1/2} \sim t^{1/2}$. When there is no longer hydrodynamic motion ($\mathbf{v} \sim 0$), which is the case here after several microseconds as seen in Fig. 5.6, the energy conservation equation $\partial\xi_3/\partial t + \nabla\cdot(\xi_3\mathbf{v}+\phi_3) = 0$ becomes $\partial\varepsilon/\partial t = -\nabla\cdot\mathbf{q}$. Using $\mathbf{q} = -\kappa\nabla T$, where κ is the neutral gas thermal conductivity, this becomes $\partial T/\partial t = \alpha\nabla^2 T$, the thermal diffusion equation, where $\alpha = \kappa/c_p$, assuming constant κ and specific heat capacity c_p. At the pressures used in our experiments, the gas dynamics are nearly ideal [83, 84] with $c_p = \frac{5}{2}Nk_B$ for a monatomic gas and $c_p = \frac{7}{2}Nk_B$ for a gas of diatomic molecules. In the temperature range achieved after repartitioning of the initial plasma energy to the neutral gas (ΔT~100 K), the thermal conduction is only very weakly dependent on temperature. For an initial Gaussian temperature distribution with a $1/e$ radius of R_0 , the solution to the thermal diffusion equation is $T(r,t) = T_0\left(\frac{R_0^2}{R_0^2+4\alpha t}\right) exp\left(\frac{-r^2}{R_0^2+4\alpha t}\right) + T_b$, where T_0 is the peak temperature and T_b is the background temperature (room temperature) of the gas. Because for our conditions the hydrodynamics has ceased after ~1 μs, the gas conforms to the pressure balance $N(r,t)T(r,t) = N_b T_b$, where N_b is the background gas density. For a relatively shallow depression, we get $\Delta N(r,t) = T_0 \frac{N_b}{T_b}\left(\frac{R_0^2}{R_0^2+4\alpha t}\right) exp\left(\frac{-r^2}{R_0^2+4\alpha t}\right)$ for the density profile, where the width varies as $\sim(R_0^2 + 4\alpha t)^{1/2}$ and the depth varies as $\sim(R_0^2 + 4\alpha t)^{-1}$, with the holes in heavier gases (smaller κ and α) expanding and decaying more slowly. For $t > R_0^2/4\alpha$ (~30 μs for R_0=50 μm and 1 atm air), the width and depth vary as $\sim(\alpha t)^{1/2}$ and $\sim(\alpha t)^{-1}$. We note that the measured long timescale density profiles for all gases investigated are very well fit by Gaussians, of which Figs. 5.4(b) and 5.5(b) are examples.

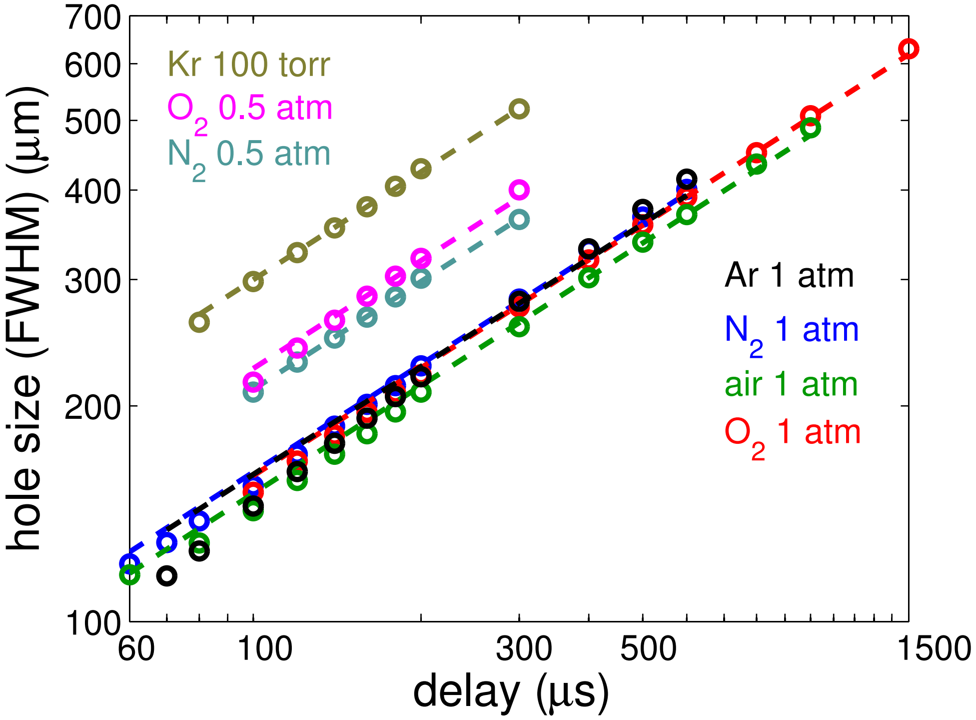

Figure 5.8 Log-log plot of measured FWHM of density hole vs. time for our range of gases and conditions. The good fit to lines of slope 1/2 verifies that the long time gas evolution is dominated by thermal diffusion.

The fact that thermal diffusion dominates the long timescale evolution of all of our tested gases is highlighted by Fig. 5.8, which is a log-log plot of measured density hole FWHM diameter vs. time for a range of gases and pressures. All points are well fitted to lines with slope 1/2 as predicted by the thermal diffusion equation. The fitted lines were used to extract the thermal diffusion coefficients α of the gases, from which the thermal conductivities were determined by $\kappa = \alpha c_p$. These are compared to the literature values in Table 4, showing good agreement.

Table 4 Thermal conductivities extracted from fits in Fig. 5.8 and comparison to literature values

gas & pressure (T=300K)	thermal conductivity κ (10^{-3}W/(m·K))	
	extracted from $\kappa = \alpha c_p$	κ from literature [83, 84]
N_2 1 atm	28.3	25.60
O_2 1 atm	27.9	26.35
air 1 atm	24.6	26.38
N_2 0.5 atm	24.0	25.59
O_2 0.5 atm	27.7	26.34
Kr 100 torr	9.1	9.28
Ar 1 atm	19.9	17.52

5.3 Discussion and conclusions

The effect of the long timescale gas density hole left by a pulse or sequence of pulses is to reduce the index of refraction near the center of the beam seen by the next pulse in the sequence. This will have a defocusing effect on the pulse. While the density profiles shown in Figs. 5.4 and 5.5 are induced by single pulses (a pump repetition rate of 20 Hz allows the density hole to completely relax between pulses), the density holes relevant to Figs. 5.1 and 5.2 have been cumulatively generated by the pulse train. Figure 5.9(a) shows a sequence of 2D density profiles for pump energy of 0.7 mJ at a repetition rate of 1 kHz in air at 1 atm. At all probe delays, the hole is significantly (~2×) deeper than for the 20 Hz pump experiment. Central lineouts of these plots are shown in Fig. 5.9(b), where here is plotted the associated refractive index shift Δn. Note that these curves are no longer well fitted by Gaussians at earlier times; thermal diffusion still dominates their evolution, but the interval between thermal source pulses is less than the single pulse dissipation time. Given that the refractive index of undisturbed atmospheric pressure air is

$\Delta n = n - 1 \sim 3\times10^{-4}$ [79], it is seen that for the conditions of Fig. 5.9, the index perturbation can be as high as $\Delta n/\delta n$ ~20%, a very big effect.

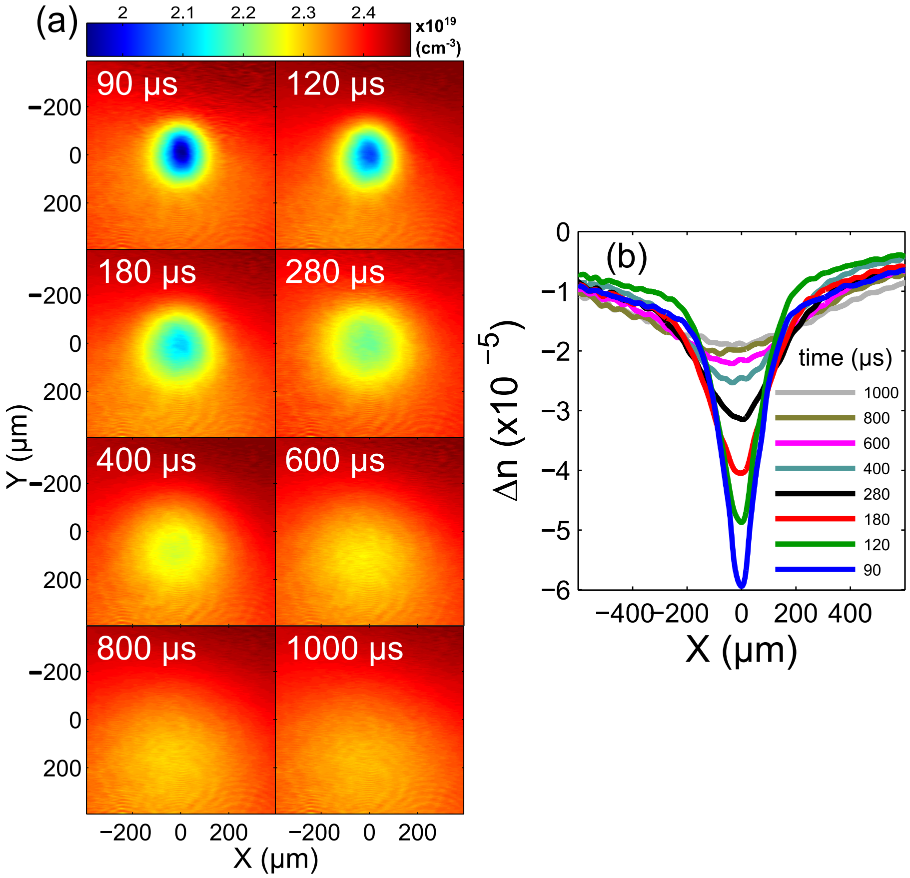

Figure 5.9 (a) Density hole profiles in 1 atm air vs. probe delay for pump pulse repetition rate of 1 kHz. (b) Central lineouts of profiles in Fig. 5.9(a). Here, the associated refractive index shift Δn is shown.

What is the effect of this on laser pulse propagation? In general, the effect of the gas density hole, especially in the highly nonlinear filamentary regime, is best understood with detailed simulations [26], which are now underway. Such simulations will help interpret the details of Figs. 5.1 and 5.2. The goal of the present chapter, however, is to present measurements of the density hole itself and some demonstrations of its effects on propagation. Below we present qualitative estimates in order to understand the main features of the propagation measurements.

For the case of a 1 kHz pulse train, the defocusing effect of the index hole on the propagating beam can be estimated using the hole refractive index shift Δn sampled across the beam, as seen in Fig. 5.9(b). The shift ranges from -10^{-6} to -10^{-5}, depending on beam diameter. For higher repetition rates or pump pulse energies, the index shifts would be even larger. The effective f-number of the density hole which contributes to beam defocusing as strongly as natural beam diffraction is $f_{\#} = \frac{1}{2}(2|\Delta n|)^{-1/2}$, giving $f_{\#}$ ~100 to ~350 for the above range of Δn. Our air filament experiment of Fig. 5.1 uses f/600 focusing, so it is clear that the cumulative density hole should have a significant defocusing influence. This is seen in Fig. 5.1, where the entire filament (initial collapse point and later termination) appears to move increasingly downstream from the lens and also lengthens with increasing pulse repetition rate. The increasing repetition rate effect of the long timescale density hole appears to be equivalent to using progressively weaker focusing lenses for filament generation. The supercontinuum generation experiment of Fig. 5.2 uses f/100 focusing, so the effect of the density hole should also be observable. This is borne out by the significant effect of repetition rate on the spectra, with appreciable blue wings added likely owing to increased filament length.

The mechanism considered thus far for gas density hole generation has been the initial plasma acting as a thermal pressure gradient source. However, another channel for laser energy deposition in gases exists, namely 2-photon Raman excitation of molecular rotation [53]. The excitation manifests itself as an ensemble average molecular alignment with respect to the pump laser polarization. The degree of alignment is expressed as $\langle\cos^2\theta\rangle_t - 1/3$ where $\langle\ \ \rangle_t$ refers to a time-dependent average over the molecular ensemble [21] and θ is the angle between the molecular axis and the laser polarization. The average alignment decays due to collisional dephasing over several hundred picoseconds in room temperature, atmospheric pressure gas [21], with the potential energy stored in the alignment being converted to thermal energy. This energy can also be the source for gas density hole generation. In other experiments [21, 48], we have measured maximum alignments $(\langle\cos^2\theta\rangle_t - 1/3)_{max}$ ~ 0.05 in nitrogen for laser intensities in the range of 5×10^{13} W/cm^2. The average energy stored per molecule in molecular alignment is roughly estimated as $u_{align} \sim \frac{1}{2}\,\gamma_{\text{eff}}^{max}\,E^2$, where E is the peak laser electric field and $\gamma_{\text{eff}}^{max} = \Delta\alpha\,(\langle\cos^2\theta\rangle_t - 1/3)_{max}$ is the maximum effective molecular polarizability under alignment, where $\Delta\alpha$ is the polarizability anisotropy [21]. For a 100 fs pulse of peak intensity 5×10^{13} W/cm^2 and $\Delta\alpha_{N_2}$=6.7×10^{-25} cm^3 [4], we get u_{align}~0.005 eV/molecule. Another estimate is obtained using our density matrix code [24] to calculate the energy invested in the rotational state population transfer excited by the pulse. This gives an average stored energy of 0.004 eV/molecule, in agreement with the alignment-based estimate above.

By comparison, an initial plasma of density N_e~2×10^{16} cm^{-3} and temperature k_BT_e~5 eV generated in atmospheric density N_2 repartitions its energy to give

~0.004 eV/molecule. So the effects are of similar size. We are currently investigating this molecular gas heating mechanism and its effect on filamentation in greater detail.

Appendix

In an isotropic medium, $\chi^{(3)}_{xxxx} = \chi^{(3)}_{yxxy} + \chi^{(3)}_{yxyx} + \chi^{(3)}_{yyxx}$ [60], where $\chi^{(3)}_{ijkl}$ is the third-order susceptibility, i is the direction of the nonlinear polarization, and the indices j, k, l are the electric field directions $(i, j, k, l = x, y, z)$. The symmetry property of the nonlinear susceptibility tensor [60] shows that in an isotropic medium $\chi^{(3)}_{yxxy} = \chi^{(3)}_{yxyx} = \chi^{(3)}_{yyxx} = \frac{1}{3}\chi^{(3)}_{xxxx}$; therefore the ratio of $\Delta\Phi_{inst}$ amplitude for the parallel and perpendicular pump-probe polarization is 3:1.

The ratio of $\Delta\Phi_{rot}$ amplitude for the parallel and perpendicular pump-probe polarization is 2:-1: here we give a brief derivation. The relative dielectric constant $\epsilon_r = n^2 = 1 + 4\pi N\langle\alpha\rangle$, where n is the refractive index, N is gas density and $\langle\alpha\rangle$ is the time-average of the second-rank linear polarizability tensor $\bar{\bar{\boldsymbol{\alpha}}}$. Because $\Delta(n^2) = 2n\Delta n = 4\pi N\Delta\langle\alpha\rangle$ and $n \approx n_0$(n_0 is the refractive index without the electric field), so $\Delta n = \frac{2\pi N}{n_0}\Delta\langle\alpha\rangle = \frac{2\pi N}{n_0}(\langle\alpha\rangle - \langle\alpha\rangle_0)$, where $\langle\alpha\rangle_0 = \frac{1}{3}(\alpha_\parallel + \alpha_\perp + \alpha_\perp) = \alpha_\perp + \frac{1}{3}\Delta\alpha$ and $\Delta\alpha = (\alpha_\parallel - \alpha_\perp)$.

Suppose the molecular axis is in the z direction, $\bar{\bar{\boldsymbol{\alpha}}} = \begin{bmatrix} \alpha_\perp & 0 & 0 \\ 0 & \alpha_\perp & 0 \\ 0 & 0 & \alpha_\parallel \end{bmatrix}$, where $\bar{\bar{\boldsymbol{\alpha}}}$ is the second order linear polarizability tensor. When the pump-probe polarization is parallel, we know that $(\langle\alpha\rangle - \langle\alpha\rangle_0)_{par.} = \Delta\alpha\left(\langle\cos^2\theta\rangle - \frac{1}{3}\right)$ [21], where θ is the angle between the molecular axis and the electric field direction, as shown in Fig. A.1.

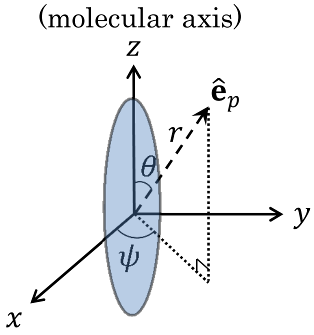

Figure A.1 The spherical coordinate showing the electric field direction and the molecular axis.

For the case of perpendicular polarization, equivalently, the $\overline{\overline{\boldsymbol{\alpha}}}$ experienced by the probe field can be written as $\overline{\overline{\boldsymbol{\alpha}}} = \begin{bmatrix} \alpha_\parallel & 0 & 0 \\ 0 & \alpha_\perp & 0 \\ 0 & 0 & \alpha_\perp \end{bmatrix}$ (or $\overline{\overline{\boldsymbol{\alpha}}} = \begin{bmatrix} \alpha_\perp & 0 & 0 \\ 0 & \alpha_\parallel & 0 \\ 0 & 0 & \alpha_\perp \end{bmatrix}$). In the spherical coordinate, the normalized pump field direction is $\hat{\mathbf{e}}_p = \begin{pmatrix} \sin\theta\cos\psi \\ \sin\theta\sin\psi \\ \cos\theta \end{pmatrix}$, so the linear polarization is $\mathbf{p} = \overline{\overline{\boldsymbol{\alpha}}}\hat{\mathbf{e}}_p = \begin{bmatrix} \alpha_\parallel & 0 & 0 \\ 0 & \alpha_\perp & 0 \\ 0 & 0 & \alpha_\perp \end{bmatrix} \begin{pmatrix} \sin\theta\cos\psi \\ \sin\theta\sin\psi \\ \cos\theta \end{pmatrix}$, thus $\langle\alpha\rangle = \mathbf{p}\cdot\hat{\mathbf{e}}_p = \left(\hat{\mathbf{e}}_p\right)^{\mathrm{T}} \overline{\overline{\boldsymbol{\alpha}}}\,\hat{\mathbf{e}}_p = \alpha_\parallel \sin^2\theta\cos^2\psi + \alpha_\perp \sin^2\theta\sin^2\psi + \alpha_\perp\cos^2\theta$. The angular average of $\cos^2\psi$ (or $\sin^2\psi$) on the x-y plane is $\int_0^{2\pi}\cos^2\psi\, d\psi/2\pi = 1/2$. Hence, when the pump-probe polarization is perpendicular, the $\langle\alpha\rangle$ experienced by the probe field is $\langle\alpha\rangle = \frac{1}{2}\alpha_\parallel\langle\sin^2\theta\rangle + \frac{1}{2}\alpha_\perp\langle\sin^2\theta\rangle + \alpha_\perp\langle\cos^2\theta\rangle = \frac{1}{2}\alpha_\parallel(1-\langle\cos^2\theta\rangle) + \frac{1}{2}\alpha_\perp(1-\langle\cos^2\theta\rangle) + \alpha_\perp\langle\cos^2\theta\rangle = -\frac{1}{2}\Delta\alpha\langle\cos^2\theta\rangle + \frac{1}{2}(\alpha_\parallel + \alpha_\perp)$,

therefore, $\langle\alpha\rangle - \langle\alpha\rangle_0 = -\frac{1}{2}\Delta\alpha\langle\cos^2\theta\rangle + \frac{1}{6}\Delta\alpha = -\frac{1}{2}\Delta\alpha\left(\langle\cos^2\theta\rangle - \frac{1}{3}\right)$, we get

$$\frac{\Delta n_{perp.}}{\Delta n_{par.}} = \frac{(\langle\alpha\rangle - \langle\alpha\rangle_0)_{perp.}}{(\langle\alpha\rangle - \langle\alpha\rangle_0)_{par.}} = -\frac{1}{2}.$$

Bibliography

1. T. Brabec, and F. Krausz, "Intense few-cycle laser fields: Frontiers of nonlinear optics," Reviews of Modern Physics **72**, 545-591 (2000).
2. A. Couairon, and A. Mysyrowicz, "Femtosecond filamentation in transparent media," Physics Reports-Review Section of Physics Letters **441**, 47-189 (2007).
3. M. Nisoli, S. DeSilvestri, O. Svelto, R. Szipocs, K. Ferencz, C. Spielmann, S. Sartania, and F. Krausz, "Compression of high-energy laser pulses below 5 fs," Optics Letters **22**, 522-524 (1997).
4. J. K. Wahlstrand, Y.-H. Cheng, and H. M. Milchberg, "Absolute measurement of the transient optical nonlinearity in N_2, O_2, N_2O, and Ar," Physical Review A **85**, 043820 (2012).
5. W. Demtröder, *Molecular physics : theoretical principles and experimental methods* (Wiley-VCH, Weinheim, 2005).
6. W. Liu, and S. L. Chin, "Direct measurement of the critical power of femtosecond Ti : sapphire laser pulse in air," Optics Express **13**, 5750-5755 (2005).
7. E. T. J. Nibbering, G. Grillon, M. A. Franco, B. S. Prade, and A. Mysyrowicz, "Determination of the inertial contribution to the nonlinear refractive index of air, N_2, and O_2 by use of unfocused high-intensity femtosecond laser pulses," Journal of the Optical Society of America B-Optical Physics **14**, 650-660 (1997).
8. M. J. Shaw, C. J. Hooker, and D. C. Wilson, "Measurement of the nonlinear refractive-index of air and other gases at 248 nm," Optics Communications **103**, 153-160 (1993).
9. J.-F. Ripoche, G. Grillon, B. Prade, M. Franco, E. Nibbering, R. Lange, and A. Mysyrowicz, "Determination of the time dependence of n_2 in air," Optics Communications **135**, 310-314 (1997).
10. V. Loriot, E. Hertz, O. Faucher, and B. Lavorel, "Measurement of high order Kerr refractive index of major air components," Optics Express **17**, 13429-13434 (2009).

11. V. Loriot, E. Hertz, O. Faucher, and B. Lavorel, "Measurement of high order Kerr refractive index of major air components: erratum," Optics Express **18**, 3011-3012 (2010).
12. D. P. Shelton, and J. E. Rice, "Measurements and calculations of the hyperpolarizabilities of atoms and small molecules in the gas phase," Chemical Reviews **94**, 3-29 (1994).
13. M. Mlejnek, E. M. Wright, and J. V. Moloney, "Dynamic spatial replenishment of femtosecond pulses propagating in air," Optics Letters **23**, 382-384 (1998).
14. J. R. Penano, P. Sprangle, B. Hafizi, A. Ting, D. F. Gordon, and C. A. Kapetanakos, "Propagation of ultra-short, intense laser pulses in air," Physics of Plasmas **11**, 2865-2874 (2004).
15. J. R. Penano, P. Sprangle, P. Serafim, B. Hafizi, and A. Ting, "Stimulated Raman scattering of intense laser pulses in air," Physical Review E **68**, 16 (2003).
16. A. Couairon, and L. Berge, "Modeling the filamentation of ultra-short pulses in ionizing media," Physics of Plasmas **7**, 193-209 (2000).
17. Y.-H. Chen, S. Varma, T. M. Antonsen, and H. M. Milchberg, "Direct Measurement of the Electron Density of Extended Femtosecond Laser Pulse-Induced Filaments," Physical Review Letters **105**, 215005 (2010).
18. N. J. Bridge, and A. D. Buckingham, "Polarization of laser light scattered by gases," Proc. R. Soc. Lond. A **295**, 334-349 (1966).
19. K. Y. Kim, I. Alexeev, and H. M. Milchberg, "Single-shot supercontinuum spectral interferometry," Applied Physics Letters **81**, 4124-4126 (2002).
20. Y.-H. Chen, S. Varma, I. Alexeev, and H. M. Milchberg, "Measurement of transient nonlinear refractive index in gases using xenon supercontinuum single-shot spectral interferometry," Optics Express **15**, 7458-7467 (2007).
21. Y.-H. Chen, S. Varma, A. York, and H. M. Milchberg, "Single-shot, space- and time-resolved measurement of rotational wavepacket revivals in H_2, D_2, N_2, O_2, and N_2O," Optics Express **15**, 11341-11357 (2007).

22. W. Liu, J. F. Gravel, F. Theberge, A. Becker, and S. L. Chin, "Background reservoir: its crucial role for long-distance propagation of femtosecond laser pulses in air," Applied Physics B-Lasers and Optics **80**, 857-860 (2005).
23. S. Varma, Y.-H. Chen, and H. M. Milchberg, "Trapping and Destruction of Long-Range High-Intensity Optical Filaments by Molecular Quantum Wakes in Air," Physical Review Letters **101**, 205001 (2008).
24. S. Varma, Y.-H. Chen, J. P. Palastro, A. B. Fallahkair, E. W. Rosenthal, T. Antonsen, and H. M. Milchberg, "Molecular quantum wake-induced pulse shaping and extension of femtosecond air filaments," Physical Review A **86**, 023850 (2012).
25. J. P. Palastro, T. M. Antonsen, Jr., S. Varma, Y.-H. Chen, and H. M. Milchberg, "Simulations of femtosecond atmospheric filaments enhanced by dual pulse molecular alignment," Physical Review A **85**, 043843 (2012).
26. J. P. Palastro, T. M. Antonsen, and H. M. Milchberg, "Compression, spectral broadening, and collimation in multiple, femtosecond pulse filamentation in atmosphere," Physical Review A **86**, 033834 (2012).
27. P. B. Corkum, C. Rolland, and T. Srinivasan-Rao, "Supercontinuum generation in gases," Physical Review Letters **57**, 2268-2271 (1986).
28. C. P. Hauri, W. Kornelis, F. W. Helbing, A. Heinrich, A. Couairon, A. Mysyrowicz, J. Biegert, and U. Keller, "Generation of intense, carrier-envelope phase-locked few-cycle laser pulses through filamentation," Applied Physics B-Lasers and Optics **79**, 673-677 (2004).
29. G. Stibenz, N. Zhavoronkov, and G. Steinmeyer, "Self-compression of millijoule pulses to 7.8 fs duration in a white-light filament," Optics Letters **31**, 274-276 (2006).
30. C. P. Hauri, R. B. Lopez-Martens, C. I. Blaga, K. D. Schultz, J. Cryan, R. Chirla, P. Colosimo, G. Doumy, A. M. March, C. Roedig, E. Sistrunk, J. Tate, J. Wheeler, L. R. DiMauro, and E. P. Power, "Intense self-compressed, self-phase-stabilized few-cycle pulses at 2 mu m from an optical filament," Optics Letters **32**, 868-870 (2007).

31. S. A. Trushin, K. Kosma, W. Fuss, and W. E. Schmid, "Sub-10-fs supercontinuum radiation generated by filamentation of few-cycle 800 nm pulses in argon," Optics Letters **32**, 2432-2434 (2007).
32. N. Zhavoronkov, "Efficient spectral conversion and temporal compression of femtosecond pulses in SF_6," Optics Letters **36**, 529-531 (2011).
33. S. Tzortzakis, B. Prade, M. Franco, A. Mysyrowicz, S. Huller, and P. Mora, "Femtosecond laser-guided electric discharge in air," Physical Review E **64**, 057401 (2001).
34. B. Forestier, A. Houard, I. Revel, M. Durand, Y. B. André, B. Prade, A. Jarnac, J. Carbonnel, M. Le Nevé, J. C. de Miscault, B. Esmiller, D. Chapuis, and A. Mysyrowicz, "Triggering, guiding and deviation of long air spark discharges with femtosecond laser filament," AIP Advances **2**, 012151 (2012).
35. V. Loriot, P. Béjot, W. Ettoumi, Y. Petit, J. Kasparian, S. Henin, E. Hertz, B. Lavorel, O. Faucher, and J. P. Wolf, "On negative higher-order Kerr effect and filamentation," Laser Physics **21**, 1319-1328 (2011).
36. P. Béjot, J. Kasparian, S. Henin, V. Loriot, T. Vieillard, E. Hertz, O. Faucher, B. Lavorel, and J. P. Wolf, "Higher-Order Kerr Terms Allow Ionization-Free Filamentation in Gases," Physical Review Letters **104**, 4 (2010).
37. D. Novoa, H. Michinel, and D. Tommasini, "Fermionic Light in Common Optical Media," Physical Review Letters **105**, 4 (2010).
38. W. Ettoumi, Y. Petit, J. Kasparian, and J. P. Wolf, "Generalized Miller Formulae," Optics Express **18**, 6613-6620 (2010).
39. J. Kasparian, P. Béjot, and J. P. Wolf, "Arbitrary-order nonlinear contribution to self-steepening," Optics Letters **35**, 2795-2797 (2010).
40. M. Kolesik, E. M. Wright, and J. V. Moloney, "Femtosecond filamentation in air and higher-order nonlinearities," Optics Letters **35**, 2550-2552 (2010).
41. P. Béjot, E. Hertz, B. Lavorel, J. Kasparian, J. P. Wolf, and O. Faucher, "From higher-order Kerr nonlinearities to quantitative modeling of third and fifth harmonic generation in argon," Optics Letters **36**, 828-830 (2011).

42. G. O. Ariunbold, P. Polynkin, and J. V. Moloney, "Third and fifth harmonic generation by tightly focused femtosecond pulses at 2.2 μm wavelength in air," Optics Express **20**, 1662-1667 (2012).
43. O. Kosareva, J.-F. Daigle, N. Panov, T. Wang, S. Hosseini, S. Yuan, G. Roy, V. Makarov, and S. L. Chin, "Arrest of self-focusing collapse in femtosecond air filaments: higher order Kerr or plasma defocusing?," Optics Letters **36**, 1035-1037 (2011).
44. P. Polynkin, M. Kolesik, E. M. Wright, and J. V. Moloney, "Experimental Tests of the New Paradigm for Laser Filamentation in Gases," Physical Review Letters **106** (2011).
45. P. Béjot, E. Hertz, J. Kasparian, B. Lavorel, J. P. Wolf, and O. Faucher, "Transition from Plasma-Driven to Kerr-Driven Laser Filamentation," Physical Review Letters **106** (2011).
46. C. Brée, A. Demircan, and G. Steinmeyer, "Saturation of the All-Optical Kerr Effect," Physical Review Letters **106**, 4 (2011).
47. A. Teleki, E. M. Wright, and M. Kolesik, "Microscopic model for the higher-order nonlinearity in optical filaments," Physical Review A **82** (2010).
48. J. K. Wahlstrand, Y.-H. Cheng, Y.-H. Chen, and H. M. Milchberg, "Optical nonlinearity in Ar and N_2 near the ionization threshold," Physical Review Letters **107**, 103901 (2011).
49. J. K. Wahlstrand, Y.-H. Cheng, and H. M. Milchberg, "High Field Optical Nonlinearity and the Kramers-Kronig Relations," Physical Review Letters **109**, 5 (2012).
50. J. K. Wahlstrand, and H. M. Milchberg, "Effect of a plasma grating on pump-probe experiments near the ionization threshold in gases," Optics Letters **36**, 3822-3824 (2011).
51. J. K. Wahlstrand, J. H. Odhner, E. T. McCole, Y.-H. Cheng, J. P. Palastro, R. J. Levis, and H. M. Milchberg, "Effect of two-beam coupling in strong-field optical pump-probe experiments," Physical Review A **87**, 13 (2013).

52. J. H. Odhner, D. A. Romanov, E. T. McCole, J. K. Wahlstrand, H. M. Milchberg, and R. J. Levis, "Ionization-Grating-Induced Nonlinear Phase Accumulation in Spectrally Resolved Transient Birefringence Measurements at 400 nm," Physical Review Letters **109**, 5 (2012).
53. D. V. Kartashov, A. V. Kirsanov, A. M. Kiselev, A. N. Stepanov, N. N. Bochkarev, Y. N. Ponomarev, and B. A. Tikhomirov, "Nonlinear absorption of intense femtosecond laser radiation in air," Optics Express **14**, 7552-7558 (2006).
54. F. Vidal, D. Comtois, C. Y. Chien, A. Desparois, B. La Fontaine, T. W. Johnston, J. C. Kieffer, H. P. Mercure, H. Pepin, and F. A. Rizk, "Modeling the triggering of streamers in air by ultrashort laser pulses," IEEE Transactions on Plasma Science **28**, 418-433 (2000).
55. W. Koechner, *Solid-state laser engineering* (Springer, New York, 2006).
56. K. Y. Kim, I. Alexeev, and H. M. Milchberg, "Single-shot measurement of laser-induced double step ionization of helium," Optics Express **10**, 1563-1572 (2002).
57. T. R. Clark, and H. M. Milchberg, "Time- and space-resolved density evolution of the plasma waveguide," Physical Review Letters **78**, 2373-2376 (1997).
58. T. R. Clark, and H. M. Milchberg, "Time-evolution and guiding regimes of the laser-produced plasma waveguide," Physics of Plasmas **7**, 2192-2197 (2000).
59. A. M. Zheltikov, "Raman response function of atmospheric air," Optics Letters **32**, 2052-2054 (2007).
60. R. L. Sutherland, D. G. McLean, and S. Kirkpatrick, *Handbook of nonlinear optics* (Marcel Dekker, New York, 2003).
61. C. Iaconis, and I. A. Walmsley, "Self-referencing spectral interferometry for measuring ultrashort optical pulses," IEEE Journal of Quantum Electronics **35**, 501-509 (1999).
62. (The nonperturbative density matrix calculation, for a 40-fs FWHM pulse and temperature of 300 K, includes rotational states up to $j_{max} = 30$ for N_2 and O_2 and $j_{max} = 45$ for N_2O).

63. C. H. Lin, J. P. Heritage, T. K. Gustafson, R. Y. Chiao, and J. P. McTague, "Birefringence arising from reorientation of polarizability anisotropy of molecules in collisionless gases," Physical Review A **13**, 813-829 (1976).
64. D. M. Bishop, "General dispersion formulas for molecular third-order nonlinear optical properties," Journal of Chemical Physics **90**, 3192-3295 (1989).
65. D. E. Laban, W. C. Wallace, R. D. Glover, R. T. Sang, and D. Kielpinski, "Self-focusing in air with phase-stabilized few-cycle light pulses," Optics Letters **35**, 1653-1655 (2010).
66. P. Whalen, J. V. Moloney, and M. Kolesik, "Self-focusing collapse distance in ultrashort pulses and measurement of nonlinear index," Optics Letters **36**, 2542-2544 (2011).
67. K. B. Macadam, and N. F. Ramsey, "Molecular-beam magnetic-resonance measurements of anisotropies of electric polarizabilities of H_2 and D_2," Physical Review A **6**, 898-906 (1972).
68. http://webbook.nist.gov/chemistry/.
69. G. Stegeman, D. G. Papazoglou, R. Boyd, and S. Tzortzakis, "Nonlinear birefringence due to non-resonant, higher-order Kerr effect in isotropic media," Optics express **19**, 6387-6399 (2011).
70. C. Marceau, S. Ramakrishna, S. Genier, T. J. Wang, Y. P. Chen, F. Theberge, M. Chateauneuf, J. Dubois, T. Seideman, and S. L. Chin, "Femtosecond filament induced birefringence in argon and in air: Ultrafast refractive index change," Optics Communications **283**, 2732-2736 (2010).
71. H. J. Lehmeier, W. Leupacher, and A. Penzkofer, "Nonresonant third order hyperpolarizability of rare gases and N_2 determined by third harmonic generation," Optics Communications **56**, 67-72 (1985).
72. J. K. Wahlstrand, Y.-H. Chen, Y.-H. Cheng, S. R. Varma, and H. M. Milchberg, "Measurements of the High Field Optical Nonlinearity and Electron Density in Gases: Application to Filamentation Experiments," IEEE Journal of Quantum Electronics **48**, 760-767 (2012).

73. S. F. J. Larochelle, A. Talebpour, and S. L. Chin, "Coulomb effect in multiphoton ionization of rare-gas atoms," Journal of Physics B-Atomic Molecular and Optical Physics **31**, 1215-1224 (1998).
74. S. Larochelle, A. Talebpour, and S. L. Chin, "Non-sequential multiple ionization of rare gas atoms in a Ti : Sapphire laser field," Journal of Physics B-Atomic Molecular and Optical Physics **31**, 1201-1214 (1998).
75. O. G. Kosareva, V. P. Kandidov, A. Brodeur, and S. L. Chin, "From filamentation in condensed media to filamentation in gases," Journal of Nonlinear Optical Physics & Materials **6**, 485-494 (1997).
76. M. V. Ammosov, N. B. Delone, and V. P. Kraĭnov, "Tunnel ionization of complex atoms and of atomic ions in an alternating electromagnetic field," Soviet Physics JETP **64**, 1191-1194 (1986).
77. P. Béjot, E. Cormier, E. Hertz, B. Lavorel, J. Kasparian, J. P. Wolf, and O. Faucher, "High-Field Quantum Calculation Reveals Time-Dependent Negative Kerr Contribution," Physical Review Letters **110**, 5 (2013).
78. S. Tzortzakis, B. Prade, M. Franco, and A. Mysyrowicz, "Time-evolution of the plasma channel at the trail of a self-guided IR femtosecond laser pulse in air," Optics Communications **181**, 123-127 (2000).
79. K. P. Birch, "Precise determination of refractometric parameters for atmospheric gases," Journal of the Optical Society of America A-Optics Image Science and Vision **8**, 647-651 (1991).
80. M. D. Feit, and J. A. Fleck, "Light-propagation in graded-index optical fibers," Applied Optics **17**, 3990-3998 (1978).
81. B. M. Smirnov, *Physics of ionized gases* (John Wiley, New York, 2001).
82. C. I. Blaga, F. Catoire, P. Colosimo, G. G. Paulus, H. G. Muller, P. Agostini, and L. F. DiMauro, "Strong-field photoionization revisited," Nature Physics **5**, 335-338 (2009).
83. http://webbook.nist.gov/chemistry/fluid/.
84. W. M. Haynes, *Handbook of Chemistry and Physics* (CRC Press, 2012).